

# CHARACTERISTIC BOUNDARY CONDITIONS FOR HYBRIDIZABLE DISCONTINUOUS GALERKIN METHODS

JAN ELLMENREICH, PHILIP L. LEDERER, MATTEO GIACOMINI, AND ANTONIO HUERTA

**ABSTRACT.** In this work we introduce the concept of characteristic boundary conditions (CBCs) within the framework of Hybridizable Discontinuous Galerkin (HDG) methods, including both the Navier-Stokes characteristic boundary conditions (NSCBCs) and a novel approach to generalized characteristic relaxation boundary conditions (GRCBCs). CBCs are based on the characteristic decomposition of the compressible Euler equations and are designed to prevent the reflection of waves at the domain boundaries. We show the effectiveness of the proposed method for weakly compressible flows through a series of numerical experiments by comparing the results with common boundary conditions in the HDG setting and reference solutions available in the literature. In particular, HDG with CBCs show superior performance minimizing the reflection of vortices at artificial boundaries, for both inviscid and viscous flows.

## 1. INTRODUCTION

The direct numerical simulation (DNS) of unsteady compressible flows, involving the simultaneous resolution of both aerodynamic and acoustic scales, commonly referred to as direct noise computation (DNC), is a challenging task in computational aeroacoustics (CAA). Accurately resolving the relevant physical scales necessitates the use of low-dissipative and low-dispersive high-order numerical methods, particularly because acoustic waves can propagate over long distances, with minimal attenuation due to viscous dissipation [1]. Furthermore, the high spatial resolution requirements call for compact and computationally efficient numerical methods, such as finite-difference (FD), high-order finite-volume (FV), and the finite-element (FE) methods. Among these, the finite-element method is particularly advantageous for handling arbitrary complex geometries using non-uniform, possibly unstructured, meshes.

In simulations, limited computational resources necessitate a trade-off between spatial resolution and the size of the computational domain, which inevitably results in domain truncation, especially in external flows. To approximate an otherwise infinite domain, artificial boundary conditions, also known as far-field, transparent or non-reflection boundary conditions, are employed to mimic the behavior of physical boundaries, and prevent spurious wave reflections from propagating back into the domain. The development of accurate and efficient boundary conditions is, therefore, essential for the success of numerical simulations, particularly in the context of compressible flows. A comprehensive review of boundary conditions for compressible flows can be found in [2, 3].

A common strategy to prevent reflections at artificial boundaries is to extend the domain by adding a buffer layer. Sponge layers [4, 5] damp the flow exponentially over time towards a target state. However, these layers are inherently reflective [2], and require to progressively increase the sponge strength to reduce reflections. More advanced techniques, such as perfectly matched layers (PML) [6, 7], are designed to be non-reflecting, although their strict application is limited to linearized problems. Despite their effectiveness, all these methods suffer the common drawback of requiring additional computational resources.

A widely used method for imposing boundary conditions is the family of characteristic boundary conditions (CBCs), based on the characteristic decomposition of the non-linear Euler equations along the local normal to the boundary. This approach leads to the well-known locally one-dimensional and inviscid (LODI) relations [8, 9, 10], which modify incoming characteristic amplitudes to prevent boundary reflections. The core concept is that, in a one-dimensional framework, wave amplitudes remain constant along characteristic lines, even in non-linear scenarios. To address the issue of the steady-state solutions depending on the initial conditions, [11]

introduced a relaxation term with user-defined parameters to accelerate convergence toward a target state. This relaxation method was further refined in a recent study [12], with the development of generalized characteristic relaxation boundary conditions (GRCBCs), which eliminated the need for user-defined parameters by incorporating a suitable Courant-Friedrichs-Lewy condition (CFL) at the boundary. The extension to viscous flows was accomplished by [13], who developed the Navier-Stokes characteristic boundary conditions (NSCBCs) through the introduction of appropriate viscous conditions. Since then, NSCBCs have been used in numerous studies [14, 15, 16, 17, 18].

Although the aforementioned characteristic boundary conditions are inherently based on a one-dimensional framework, incorporating multidimensional effects is essential for accurately capturing complex flow phenomena. In [14], the authors extend NSCBCs by introducing damped convective transverse gradients through a transverse relaxation factor  $\beta$ . The value of  $\beta$  was determined via a low Mach number asymptotic analysis of the Euler equations. However, identifying the optimal value for  $\beta$  remains an active area of research [15, 16, 19, 17].

In the literature, the implementation of CBCs is often confined to FD methods, since the modified characteristic system is solely solved for the boundary nodes. However, in the finite element context, specifically for the Discontinuous Galerkin (DG) and Hybridizable Discontinuous Galerkin (HDG) methods, boundary conditions are enforced in a weak sense through numerical fluxes  $\hat{\mathbf{F}}$  [20, 21, 22]. This approach requires an explicit external boundary state  $\mathbf{U}^-$ . To our knowledge, only two studies have addressed this issue within the DG framework. In [23], the authors introduced mirror elements adjacent to the boundary elements, where the modified characteristic system is solved to determine  $\mathbf{U}^-$ . In [24, 25], the authors imposed the characteristic wave amplitudes and determined the external boundary state  $\mathbf{U}^-$  via a least-squares approach by exploiting the discrete differential operator of the nodal shape functions.

HDG methods have gained significant popularity for simulating compressible flows in recent years [26, 27, 28]. These methods effectively combine the benefits of DG approaches — such as local conservation, high-order spatial accuracy, and the capability to manage complex geometries — while offering potential reductions in computational costs, particularly in scenarios, involving implicit time stepping. This cost reduction is achieved by introducing appropriate traces of the unknowns on the mesh skeleton, significantly reducing the global coupling of degrees of freedom. This decoupling is especially beneficial as it facilitates the use of techniques like static condensation to eliminate the elemental degrees of freedom [29].

This work extends the concept of characteristic boundary conditions (CBCs) within the HDG framework, encompassing both the Navier-Stokes characteristic boundary conditions (NSCBCs) and a novel approach to generalized characteristic relaxation boundary conditions (GRCBCs).

In Section 2 we give an overview of the compressible Navier-Stokes equations with particular emphasis on the derivation of the characteristic quasi-linear form of the Euler equations. We then introduce the fundamental concept of CBCs, including NSCBCs and GRCBCs, with a particular focus on their application to subsonic inflows and outflows.

In the subsequent Section 3, we introduce the finite element notation, the discrete variational formulation of the mixed HDG method for compressible viscous flows, and some common boundary conditions. Additionally, we propose a slight modification of the far-field boundary condition, which showed numerical stability improvements in our experiments.

Then, in Section 4, we give a detailed explanation of CBCs implementation within the HDG framework, where we first consider the one-dimensional inviscid setting (LODI) and then extend it to the multidimensional and viscous setting. Additionally, we introduce a novel approach to GRCBCs and show that common HDG boundary conditions can be recovered as a special case of the proposed method. In contrast to the DG implementations, our implementation does not rely on additional mirror elements or nodal shape functions, and can be naturally embedded into the numerical method.

Section 5 shows the effectiveness of the proposed method through a series of numerical experiments including a linear acoustic pulse, a non-linear oblique pressure pulse, a zero-circulation vortex, and a laminar viscous flow around a cylinder. We evaluate the performance of CBCs by comparing the results with the traditional boundary conditions and reference or exact solutions.

Our focus lies on weakly compressible flows, i.e. Mach number  $\text{Ma}_\infty \leq 0.3$ , and the assessment of subsonic inflow and outflow boundary conditions.

Ultimately, in Section 6 we summarize our findings.

## 2. COMPRESSIBLE FLOW EQUATIONS AND CHARACTERISTIC BOUNDARY CONDITIONS

The fundamental equations describing the motion of an unsteady, viscous compressible flow in a space-time cylinder  $\Omega \times (0, t_{\text{end}}] \in \mathbb{R}^{d+1}$  with non-empty, bounded,  $d$ -dimensional spatial domain  $\Omega$ , with boundary  $\partial\Omega$ , and final time  $t_{\text{end}}$ , are specified by the compressible Navier-Stokes equations. In terms of conservative variables,  $\mathbf{U} = (\rho, \rho\mathbf{u}, \rho E)^\top$ , with density  $\rho$ , velocity  $\mathbf{u}$ , and total specific energy  $E$ , this system can be expressed in dimensionless form as

$$(1) \quad \frac{\partial \mathbf{U}}{\partial t} + \text{div}(\mathbf{F}(\mathbf{U}) - \mathbf{G}(\mathbf{U}, \boldsymbol{\varepsilon}, \boldsymbol{\phi})) = \mathbf{0} \quad \text{in } \Omega \times (0, t_{\text{end}}],$$

by applying either an aerodynamic or an acoustic scaling with the reference values

$$(2a) \quad (\text{aerodynamic}) \quad \rho_{\text{ref}} := \rho_\infty^*, \quad u_{\text{ref}} := |\mathbf{u}_\infty^*|, \quad \theta_{\text{ref}} := \theta_\infty^*(\gamma - 1)\text{Ma}_\infty^2,$$

$$(2b) \quad (\text{acoustic}) \quad \rho_{\text{ref}} := \rho_\infty^*, \quad u_{\text{ref}} := c_\infty^*, \quad \theta_{\text{ref}} := \theta_\infty^*(\gamma - 1),$$

depending on the flow regime under consideration, where  $\theta$  and  $c$  denote the temperature and speed of sound, respectively. Note that dimensional values are marked by an asterisk. With the Mach number  $\text{Ma}_\infty$ , the Reynolds number  $\text{Re}_\infty$  and the Prandtl number  $\text{Pr}_\infty$  defined as

$$\text{Ma}_\infty := \frac{|\mathbf{u}_\infty^*|}{c_\infty^*}, \quad \text{Re}_\infty := \frac{u_{\text{ref}} \rho_\infty^* L^*}{\mu_\infty^*}, \quad \text{Pr}_\infty := \frac{\mu_\infty^* c_p}{\kappa_\infty^*},$$

the convective and the viscous fluxes are given by

$$(3) \quad \mathbf{F}(\mathbf{U}) = \begin{pmatrix} \rho\mathbf{u}^\top \\ \rho\mathbf{u} \otimes \mathbf{u} + p\mathbf{I} \\ \rho H\mathbf{u}^\top \end{pmatrix}, \quad \mathbf{G}(\mathbf{U}, \boldsymbol{\varepsilon}, \boldsymbol{\phi}) = \frac{1}{\text{Re}_\infty} \begin{pmatrix} \mathbf{0}^\top \\ 2\boldsymbol{\varepsilon} \\ (2\boldsymbol{\varepsilon}\mathbf{u} + \boldsymbol{\phi}/\text{Pr}_\infty)^\top \end{pmatrix},$$

respectively, where  $p$  denotes the pressure,  $H = E + p/\rho$  the specific enthalpy,  $\boldsymbol{\varepsilon}$  the rate-of-strain tensor,  $\boldsymbol{\phi} = \nabla\theta$  the temperature gradient,  $\mu$  the dynamic viscosity,  $c_p$  the specific heat capacity,  $\kappa$  the thermal conductivity and  $L$  a characteristic length.

To close the system of equations (1) we assumed a Newtonian fluid, defined by a linear relationship between the rate-of-strain tensor  $\boldsymbol{\varepsilon}$ , given by

$$(4) \quad \boldsymbol{\varepsilon} := \frac{\nabla\mathbf{u} + (\nabla\mathbf{u})^\top}{2} - \frac{1}{3}\text{div}(\mathbf{u})\mathbf{I},$$

and the deviatoric stress tensor  $\boldsymbol{\tau}$ , namely,

$$(5) \quad \boldsymbol{\tau} = \frac{2\boldsymbol{\varepsilon}}{\text{Re}_\infty}.$$

Additionally, we assumed that the heat flux,  $\mathbf{q}$ , obeys Fourier's law of heat conduction, i.e.

$$(6) \quad \mathbf{q} = -\frac{\boldsymbol{\phi}}{\text{Re}_\infty \text{Pr}_\infty}.$$

Lastly, we assumed ideal gas conditions given by the equation of state

$$(7) \quad \gamma p = \rho(\gamma - 1)\theta,$$

with heat capacity ratio  $\gamma = 1.4$  for air. In this setting the isentropic speed of sound  $c$  is defined as

$$(8) \quad c = \sqrt{\gamma \frac{p}{\rho}} = \sqrt{(\gamma - 1)\theta}.$$

The velocity  $\mathbf{u}$ , the pressure  $p$  and the temperature  $\theta$  can be expressed in terms of the conservative variables  $\mathbf{U}$  as follows:

$$(9) \quad \mathbf{u}(\mathbf{U}) := \frac{\rho\mathbf{u}}{\rho}, \quad p(\mathbf{U}) := (\gamma - 1) \left( \rho E - \frac{|\rho\mathbf{u}|^2}{2\rho} \right), \quad \theta(\mathbf{U}) := \gamma \left( \frac{\rho E}{\rho} - \frac{|\rho\mathbf{u}|^2}{2\rho^2} \right).$$

Throughout this work we assume a two-dimensional setting<sup>1</sup> with a local orthogonal coordinate system  $(\xi, \eta)$ , relatively oriented with respect to the global Cartesian coordinate system  $(x, y)$  as shown in Figure 1. We introduce the orthonormal basis vectors  $(\mathbf{n}, \mathbf{t})$  and define the corresponding projection of the velocity  $\mathbf{u}$  onto these basis vectors as follows

$$(10) \quad u_n = \mathbf{u} \cdot \mathbf{n} = u_x n_x + u_y n_y, \quad u_t = \mathbf{u} \cdot \mathbf{t} = u_x t_x + u_y t_y.$$

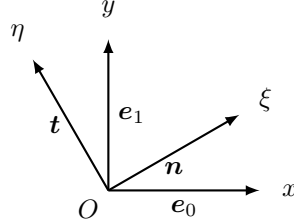


FIGURE 1. Local orthogonal coordinate system  $(\xi, \eta)$  with the orthonormal basis vectors  $\mathbf{n}$  and  $\mathbf{t}$ .

**2.1. Characteristic form of the governing equations.** The hyperbolic nature of the Navier-Stokes equations (1) with respect to time lies in the Euler equations [30],

$$(11) \quad \frac{\partial \mathbf{U}}{\partial t} + \operatorname{div}(\mathbf{F}(\mathbf{U})) = \mathbf{0},$$

which are derived by neglecting the viscous contributions. From a characteristic point of view, it is essential to express these equations in quasi-linear form

$$(12) \quad \frac{\partial \mathbf{U}}{\partial t} + \mathbf{A} \frac{\partial \mathbf{U}}{\partial \xi} + \mathbf{B} \frac{\partial \mathbf{U}}{\partial \eta} = \mathbf{0},$$

where the convective Jacobians given are defined as [31]

$$(13a) \quad \mathbf{A} := \frac{\partial(\mathbf{F}\mathbf{n})}{\partial \mathbf{U}} = \begin{pmatrix} 0 & n_x & n_y & 0 \\ \frac{\gamma-1}{2}|\mathbf{u}|^2 n_x - u_x u_n & u_n - (\gamma-2)u_x n_x & u_x n_y - (\gamma-1)u_y n_x & (\gamma-1)n_x \\ \frac{\gamma-1}{2}|\mathbf{u}|^2 n_y - u_y u_n & u_y n_x - (\gamma-1)u_x n_y & u_n - (\gamma-2)u_y n_y & (\gamma-1)n_y \\ (\frac{\gamma-1}{2}|\mathbf{u}|^2 - H)u_n & Hn_x - (\gamma-1)u_x u_n & Hn_y - (\gamma-1)u_y u_n & \gamma u_n \end{pmatrix},$$

$$(13b) \quad \mathbf{B} := \frac{\partial(\mathbf{F}\mathbf{t})}{\partial \mathbf{U}} = \begin{pmatrix} 0 & t_x & t_y & 0 \\ \frac{\gamma-1}{2}|\mathbf{u}|^2 t_x - u_x u_t & u_t - (\gamma-2)u_x t_x & u_x t_y - (\gamma-1)u_y t_x & (\gamma-1)t_x \\ \frac{\gamma-1}{2}|\mathbf{u}|^2 t_y - u_y u_t & u_y t_x - (\gamma-1)u_x t_y & u_t - (\gamma-2)u_y t_y & (\gamma-1)t_y \\ (\frac{\gamma-1}{2}|\mathbf{u}|^2 - H)u_t & Ht_x - (\gamma-1)u_x u_t & Ht_y - (\gamma-1)u_y u_t & \gamma u_t \end{pmatrix}.$$

Unfortunately, the convective Jacobians  $\mathbf{A}$  and  $\mathbf{B}$  cannot be simultaneously diagonalized. This arises from the fact that, in a multidimensional framework, waves can propagate in infinitely many directions, and characteristic variables may not remain constant along characteristic lines [32, 17].

<sup>1</sup>Every derivation can be extended to the three-dimensional case; however, we focus on the two-dimensional case for the sake of clarity and readability.

Nevertheless, a characteristic decomposition of  $\mathbf{A}$  can be performed to obtain the eigenvalues  $\mathbf{\Lambda}$  and eigenvectors  $\mathbf{P}$ , defined as follows

$$(14a) \quad \mathbf{\Lambda} := \text{diag}(\lambda_0, \lambda_1, \lambda_2, \lambda_3) = \text{diag}(u_n - c, u_n, u_n, u_n + c),$$

$$(14b) \quad \mathbf{P} := \begin{pmatrix} \frac{1}{2c^2} & \frac{1}{c^2} & 0 & \frac{1}{2c^2} \\ -\frac{n_x}{2c} + \frac{u_x}{2c^2} & \frac{u_x}{c^2} & \rho n_y & \frac{n_x}{2c} + \frac{u_x}{2c^2} \\ -\frac{n_y}{2c} + \frac{u_y}{2c^2} & \frac{u_y}{c^2} & -\rho n_x & \frac{n_y}{2c} + \frac{u_y}{2c^2} \\ \frac{1}{2(\gamma-1)} - \frac{u_n}{2c} + \frac{|\mathbf{u}|^2}{4c^2} & \frac{|\mathbf{u}|^2}{2c^2} & \rho u_x n_y - \rho u_y n_x & \frac{1}{2(\gamma-1)} + \frac{u_n}{2c} + \frac{|\mathbf{u}|^2}{4c^2} \end{pmatrix},$$

$$(14c) \quad \mathbf{P}^{-1} := \begin{pmatrix} c u_n + \frac{\gamma-1}{2} |\mathbf{u}|^2 & -c n_x + u_x(1-\gamma) & -c n_y + u_y(1-\gamma) & \gamma - 1 \\ c^2 - \frac{\gamma-1}{2} |\mathbf{u}|^2 & -u_x(1-\gamma) & -u_y(1-\gamma) & 1 - \gamma \\ -\frac{u_x n_y}{\rho} + \frac{u_y n_x}{\rho} & \frac{n_y}{\rho} & -\frac{n_x}{\rho} & 0 \\ -c u_n + \frac{\gamma-1}{2} |\mathbf{u}|^2 & c n_x + u_x(1-\gamma) & c n_y + u_y(1-\gamma) & \gamma - 1 \end{pmatrix},$$

By definition of eigendecomposition, it holds that  $\mathbf{A} = \mathbf{P}\mathbf{\Lambda}\mathbf{P}^{-1}$ , although the choice of eigenvectors  $\mathbf{P}$  is not unique. Furthermore, the eigenvalues  $\mathbf{\Lambda}$ , and consequently the convective Jacobian  $\mathbf{A}$ , can be decomposed based on the sign of the eigenvalues

$$(15) \quad \mathbf{\Lambda} = \mathbf{\Lambda}^- + \mathbf{\Lambda}^+, \quad \mathbf{\Lambda}^\mp := \frac{\mathbf{\Lambda} \mp |\mathbf{\Lambda}|}{2}, \quad \mathbf{A}^\mp := \mathbf{P}\mathbf{\Lambda}^\mp\mathbf{P}^{-1}.$$

Additionally, we introduce the closely related identities and their projections onto the eigenvectors

$$(16) \quad \mathbf{I} = \mathbf{I}^- + \mathbf{I}^+, \quad \mathbf{I}^\mp := \frac{\mathbf{I} \mp \mathbf{I}_n}{2}, \quad \mathbf{Q}^\mp := \mathbf{P}\mathbf{I}^\mp\mathbf{P}^{-1},$$

where  $\mathbf{I}_n$  is defined as

$$(17) \quad \mathbf{I}_n := \text{diag}(I_0, I_1, I_2, I_3), \quad I_i = \begin{cases} 1 & \lambda_i > 0, \\ 0 & \lambda_i = 0, \\ -1 & \lambda_i < 0. \end{cases}$$

For the remainder of this work, the basis vector  $\mathbf{n}$  is assumed to represent the outward unit normal vector at any arbitrary boundary. Consequently, the basis vector  $\mathbf{t}$  is the unit tangential vector, obtained by rotating  $\mathbf{n}$  counterclockwise. With these definitions, we can classify the eigenvalues  $\mathbf{\Lambda}^\mp$  as the speeds of incoming and outgoing waves, respectively. Additionally, the Jacobians  $\mathbf{A}^-$  and  $\mathbf{A}^+$  are referred to as the incoming and outgoing convective Jacobians, while the identities  $\mathbf{I}^-$  and  $\mathbf{I}^+$  are referred to as the incoming and outgoing identities.

Notably, in the special case of  $\mathbf{I}_n = \mathbf{0}$ , the incoming and outgoing identities reduce to  $\mathbf{I}^\mp = \frac{1}{2}\mathbf{I}$ , ensuring that both contributions are retained.

The characteristic form of the Euler equations is obtained by premultiplying the system of equations (12) by the left eigenvectors  $\mathbf{P}^{-1}$ , while exploiting the identity  $\mathbf{P}\mathbf{P}^{-1} = \mathbf{I}$ . This procedure leads to

$$\begin{aligned} \mathbf{P}^{-1} \frac{\partial \mathbf{U}}{\partial t} + \mathbf{P}^{-1} \mathbf{A} \frac{\partial \mathbf{U}}{\partial \xi} + \mathbf{P}^{-1} \mathbf{B} \frac{\partial \mathbf{U}}{\partial \eta} &= \mathbf{P}^{-1} \frac{\partial \mathbf{U}}{\partial t} + \mathbf{P}^{-1} \mathbf{A} \mathbf{P} \mathbf{P}^{-1} \frac{\partial \mathbf{U}}{\partial \xi} + \mathbf{P}^{-1} \mathbf{B} \mathbf{P} \mathbf{P}^{-1} \frac{\partial \mathbf{U}}{\partial \eta} \\ &= \mathbf{P}^{-1} \frac{\partial \mathbf{U}}{\partial t} + \mathbf{\Lambda} \mathbf{P}^{-1} \frac{\partial \mathbf{U}}{\partial \xi} + \mathbf{\Theta} \mathbf{P}^{-1} \frac{\partial \mathbf{U}}{\partial \eta} = \mathbf{0}, \end{aligned}$$

with

$$(18) \quad \mathbf{\Theta} := \mathbf{P}^{-1} \mathbf{B} \mathbf{P} = \begin{pmatrix} u_t & 0 & -\rho c^2 & 0 \\ 0 & u_t & 0 & 0 \\ -\frac{1}{2\rho} & 0 & u_t & -\frac{1}{2\rho} \\ 0 & 0 & -\rho c^2 & u_t \end{pmatrix}.$$

We introduce the characteristic variables  $\delta\mathbf{W}$ , which correspond to the eigenvalues  $\Lambda$  and are expressed in terms of variations as

$$(19) \quad \delta\mathbf{W} = \mathbf{P}^{-1}\delta\mathbf{U} = \begin{pmatrix} \delta p - \rho c \delta\mathbf{u} \cdot \mathbf{n} \\ c^2 \delta\rho - \delta p \\ -\delta\mathbf{u} \cdot \mathbf{t} \\ \delta p + \rho c \delta\mathbf{u} \cdot \mathbf{n} \end{pmatrix}.$$

Here the first and last characteristic variables,  $\delta\mathbf{W}_0$  and  $\delta\mathbf{W}_3$ , correspond to acoustic waves traveling upstream and downstream with speeds  $u_n - c$  and  $u_n + c$ , respectively. The remaining characteristic variables  $\delta\mathbf{W}_1$  and  $\delta\mathbf{W}_2$  are associated with entropy and vorticity waves, which are convected by the flow with velocity  $u_n$ .

With these definitions, the characteristic form of the Euler equations can be written in compact notation as

$$(20) \quad \frac{\partial\mathbf{W}}{\partial t} + \Lambda \frac{\partial\mathbf{W}}{\partial\xi} + \Theta \frac{\partial\mathbf{W}}{\partial\eta} = \mathbf{0}.$$

By neglecting the tangential contributions  $\Theta\partial\mathbf{W}/\partial\eta$ , the system decouples into  $(d+2)$  independent equations,

$$(21) \quad \frac{\partial\mathbf{W}}{\partial t} + \Lambda \frac{\partial\mathbf{W}}{\partial\xi} = \mathbf{0},$$

which, rewritten in terms of the incoming and outgoing characteristic variables  $\delta\mathbf{W}^\mp := \mathbf{I}^\mp \delta\mathbf{W}$ , reads as

$$(22) \quad \frac{\partial\mathbf{W}^\mp}{\partial t} + \Lambda^\mp \frac{\partial\mathbf{W}^\mp}{\partial\xi} = \mathbf{0}.$$

*Remark 2.1.* Premultiplying equation (21) by  $\mathbf{I}^\mp$  effectively acts as a filter, isolating the corresponding wave component.

From the theory of hyperbolic systems, it is well-established that in the simplified one-dimensional case, the characteristic variables  $\delta\mathbf{W}_i$  remain constant along the characteristic lines  $d\xi/dt = \lambda_i$ . However, as noted earlier, in a multidimensional context, the eigenvectors  $\mathbf{P}$  fail to diagonalize the tangential convective Jacobian  $\mathbf{B}$ , resulting in a non-diagonal matrix  $\Theta$ . The off-diagonal terms in  $\Theta$  act as source terms and introduce coupling between the characteristic variables  $\delta\mathbf{W}$ . Consequently, in a multidimensional setting, the characteristic quantities do not remain constant along characteristic lines derived from the simplified system of equations (21).

By repeating the above procedure for the full set of equations (1) we obtain the characteristic form of the Navier-Stokes equations

$$(23) \quad \frac{\partial\mathbf{W}}{\partial t} + \Lambda \frac{\partial\mathbf{W}}{\partial\xi} + \Theta \frac{\partial\mathbf{W}}{\partial\eta} = \mathbf{P}^{-1}\mathcal{V},$$

where the viscous contributions are defined as

$$(24) \quad \mathcal{V} := \operatorname{div}(\mathbf{G}(\mathbf{U}, \varepsilon, \phi)) = \frac{\partial(\mathbf{G}\mathbf{n})}{\partial\xi} + \frac{\partial(\mathbf{G}\mathbf{t})}{\partial\eta}.$$

Note that, rigorously speaking, the term *characteristic* is not appropriate due to the elliptic nature of the viscous terms  $\mathcal{V}$  [13].

**2.2. Navier-Stokes characteristic boundary conditions.** For the development of time-dependent boundary conditions, particularly non-reflective boundary conditions, the characteristic Navier-Stokes system (23) has been widely used in literature [13, 14, 9, 10, 33, 16]. This approach is commonly referred to as characteristic Navier-Stokes boundary conditions (NSCBCs). The system of equations (23) is often reformulated in terms of characteristic amplitudes  $\mathcal{L}$  and transverse convective contributions  $\mathcal{T}$  as follows:

$$(25) \quad \frac{\partial\mathbf{W}}{\partial t} + \mathcal{L} + \mathcal{T} = \mathbf{P}^{-1}\mathcal{V},$$

where the terms  $\mathcal{L}$  and  $\mathcal{T}$  are defined as

$$(26a) \quad \mathcal{L} := \Lambda \frac{\partial \mathbf{W}}{\partial \xi} = \begin{pmatrix} (u_n - c) \left[ \frac{\partial p}{\partial \xi} - \rho c \frac{\partial \mathbf{u}}{\partial \xi} \cdot \mathbf{n} \right] \\ u_n \left[ c^2 \frac{\partial \rho}{\partial \xi} - \frac{\partial p}{\partial \xi} \right] \\ u_n \left[ -\frac{\partial \mathbf{u}}{\partial \xi} \cdot \mathbf{t} \right] \\ (u_n + c) \left[ \frac{\partial p}{\partial \xi} + \rho c \frac{\partial \mathbf{u}}{\partial \xi} \cdot \mathbf{n} \right] \end{pmatrix} = \begin{pmatrix} \mathcal{L}_{acou} \\ \mathcal{L}_{ent} \\ \mathcal{L}_{vort} \\ \mathcal{L}_{acou} \end{pmatrix},$$

$$(26b) \quad \mathcal{T} := \Theta \frac{\partial \mathbf{W}}{\partial \eta} = \begin{pmatrix} u_t \left[ \frac{\partial p}{\partial \eta} - \rho c \frac{\partial \mathbf{u}}{\partial \eta} \cdot \mathbf{n} \right] + \rho c^2 \frac{\partial \mathbf{u}}{\partial \eta} \cdot \mathbf{t} \\ u_t \left[ c^2 \frac{\partial \rho}{\partial \eta} - \frac{\partial p}{\partial \eta} \right] \\ u_t \left[ -\frac{\partial \mathbf{u}}{\partial \eta} \cdot \mathbf{t} \right] - \frac{1}{\rho} \frac{\partial p}{\partial \eta} \\ u_t \left[ \frac{\partial p}{\partial \eta} + \rho c \frac{\partial \mathbf{u}}{\partial \eta} \cdot \mathbf{n} \right] + \rho c^2 \frac{\partial \mathbf{u}}{\partial \eta} \cdot \mathbf{t} \end{pmatrix}.$$

By further decoupling the characteristic amplitudes  $\mathcal{L}$  and transverse convective contributions  $\mathcal{T}$  into incoming and outgoing contributions, we have

$$(27a) \quad \mathcal{L} = \mathcal{L}^- + \mathcal{L}^+, \quad \mathcal{L}^\mp := \Lambda^\mp \frac{\partial \mathbf{W}}{\partial \xi},$$

$$(27b) \quad \mathcal{T} = \mathcal{T}^- + \mathcal{T}^+, \quad \mathcal{T}^\mp := I^\mp \Theta \frac{\partial \mathbf{W}}{\partial \eta}.$$

Thus, the system of equations can be expressed as

$$(28) \quad \frac{\partial \mathbf{W}}{\partial t} + \mathcal{L}^- + \mathcal{L}^+ + \mathcal{T}^- + \mathcal{T}^+ = \mathbf{P}^{-1} \mathbf{v}.$$

To ensure a well-posed problem, it is essential from a physical standpoint to specify the incoming wave information on artificial boundaries. The NSCBC approach models the incoming amplitudes  $\mathcal{L}^-$  and appropriately relaxes the transverse terms  $\mathcal{T}^-$  in equation (28), which contribute to the time evolution of the incoming characteristic wave  $\delta \mathbf{W}^-$ . Therefore, we rewrite the system of equations (28) as

$$(29) \quad \frac{\partial \mathbf{W}}{\partial t} + \tilde{\mathcal{L}}^- + \mathcal{L}^+ + \beta \mathcal{T}^- + \mathcal{T}^+ = \mathbf{P}^{-1} \mathbf{v},$$

where  $\tilde{\mathcal{L}}^-$  denotes the modeled incoming characteristic amplitudes and  $\beta > 0$  is a relaxation coefficient for the transverse contribution. It is important to note that for outgoing waves  $\delta \mathbf{W}^+$  no modeling is necessary, as they are determined by the conditions prevailing within the interior.

The incoming characteristic amplitudes  $\mathcal{L}^-$  are typically approximated by assuming a relaxation toward a given target state  $\mathbf{U}^-$ . By applying a first-order, one-sided upwind finite-difference scheme along a characteristic length  $L$ , an approximation to the derivative is obtained:

$$(30) \quad \frac{\partial \mathbf{W}}{\partial \xi} \stackrel{\text{FD approx.}}{\approx} -\mathbf{P}^{-1} \frac{\mathbf{U} - \mathbf{U}^-}{L}.$$

Consequently, the modeled incoming characteristic amplitudes  $\tilde{\mathcal{L}}^-$  are obtained by inserting the above approximation into equation (27a)

$$(31) \quad \mathcal{L}^- \approx \tilde{\mathcal{L}}^- := \mathbf{D}^- \mathbf{P}^{-1} (\mathbf{U} - \mathbf{U}^-),$$

where a positive diagonal eigenvalue-like relaxation matrix is introduced:

$$(32) \quad \mathbf{D}^- \sim -\frac{1}{L} \Lambda^-.$$

The precise definition of the relaxation matrix depends on the specific type of boundary condition and will be addressed in the following sections.

Once the modeled characteristic amplitudes  $\tilde{\mathcal{L}}^-$  and the transverse relaxation coefficient  $\beta$  are defined, the time-dependent problem described by equation (29) is solved at the boundary.

In a viscous setting, the authors of [13] propose to modify the viscous contributions  $\mathbf{V}$  in the conservative equations (29) by appropriate viscous conditions. Usually, these modifications include a zero-normal gradient condition for a stress component  $\tau_{ij}$  and/or a zero-normal gradient condition for a heat flux component  $q_i$  as these conditions gradually transition to the inviscid state when viscosity and conductivity approach zero.

*Remark 2.2.* To properly impose the modeled characteristic amplitudes  $\tilde{\mathcal{L}}^-$ , it is necessary to specify both the target state  $\mathbf{U}^-$  and the relaxation matrix  $\mathbf{D}^-$ , depending on the specific Mach regime and the type of boundary condition being applied. While selecting the target state is generally straightforward based on the boundary condition type, the relaxation matrix typically contains parameters that may require tuning to suit the specific circumstances. Additionally, the value of the tangential relaxation parameter  $\beta \sim \mathcal{O}(1)$  must be adjusted accordingly.

It is worth noticing that, by neglecting tangential and viscous contributions in (29), we recover the locally one-dimensional inviscid (LODI) approach, given by:

$$(33) \quad \frac{\partial \mathbf{W}}{\partial t} + \tilde{\mathcal{L}}^- + \mathcal{L}^+ = \mathbf{0}.$$

While the LODI framework (33) offers computational efficiency due to the decoupling of the characteristic variables, the one-dimensional inviscid assumption may be too restrictive for modeling multidimensional flows. This is because it oversimplifies the complex interactions that occur in flows with variations across multiple dimensions.

In the following subsections, we present examples of boundary conditions for subsonic inflow and outflow conditions, which are based on the NSCBC framework.

**2.2.1. Subsonic outflow.** For a subsonic outflow, ensuring well-posedness requires specifying a single physical boundary condition, typically the target pressure  $p_\infty$ . However, imposing this pressure strongly can lead to unwanted reflections at the boundary. A more consistent approach from the physical standpoint consists of modeling the single characteristic wave of purely acoustic nature entering the domain from downstream

$$(34) \quad \mathcal{L}_{outflow}^- := \begin{pmatrix} \mathcal{L}_{acou} \\ 0 \\ 0 \\ 0 \end{pmatrix} = \begin{pmatrix} (u_n - c) \left[ \frac{\partial p}{\partial \xi} - \rho c \frac{\partial \mathbf{u}}{\partial \xi} \cdot \mathbf{n} \right] \\ 0 \\ 0 \\ 0 \end{pmatrix}.$$

A schematic representation of the characteristic amplitudes  $\mathcal{L}$  for a domain  $\Omega$  is shown in Figure 2.

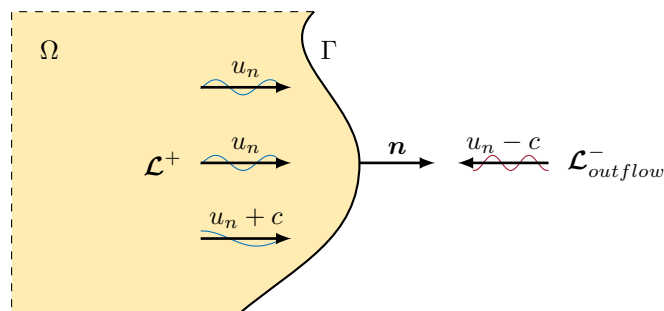


FIGURE 2. Schematic representation of the incoming,  $\mathcal{L}_{outflow}^-$ , and outgoing,  $\mathcal{L}^+$ , characteristic amplitudes at a subsonic outflow boundary  $\Gamma$ .

A widely used boundary condition [11, 13, 14] models the incoming acoustic amplitude  $\mathcal{L}_{outflow}^-$  as:

$$(35) \quad \mathcal{L}_{outflow}^- \approx \tilde{\mathcal{L}}_{outflow}^- = \begin{pmatrix} D_p(p - p_\infty) \\ 0 \\ 0 \\ 0 \end{pmatrix},$$

where the relaxation matrix  $\mathbf{D}^-$  is given by:

$$(36) \quad \mathbf{D}^- = \begin{pmatrix} D_p & 0 & 0 & 0 \\ 0 & 0 & 0 & 0 \\ 0 & 0 & 0 & 0 \\ 0 & 0 & 0 & 0 \end{pmatrix}.$$

The pressure difference  $(p - p_\infty)$  ensures relaxation toward the target pressure  $p_\infty$ . A specific form of the relaxation factor  $D_p$  was introduced in [11]:

$$(37) \quad D_p := \frac{c(1 - \text{Ma}_\infty^2)\sigma}{L},$$

where  $L$  is a characteristic length and  $\sigma > 0$  is a non-negative constant. The optimal value of  $\sigma$  was determined to be  $\sigma_{opt} \approx 0.28$ , [11, 25], though different values have been reported in the literature depending on the test case. A vanishing constant,  $\sigma = 0$ , results in a perfectly non-reflecting boundary in a one-dimensional setting but entails a drift from the target pressure  $p_\infty$ , as no information propagates upstream. Conversely, as the constant  $\sigma$  increases significantly,  $\sigma \gg 0$ , the boundary becomes stiffer and more reflective.

If incoming tangential effects are non-negligible, such as in the wake of a bluff body, the inclusion of appropriately damped tangential contributions can significantly improve the non-reflecting behavior of an outflow boundary. These contributions can be modeled as follows:

$$(38) \quad \mathcal{T}^- = \begin{pmatrix} \mathcal{T}_{acou}^- \\ 0 \\ 0 \\ 0 \end{pmatrix} = \begin{pmatrix} u_t \left[ \frac{\partial p}{\partial \eta} - \rho c \frac{\partial \mathbf{u}}{\partial \eta} \cdot \mathbf{n} \right] + \rho c^2 \frac{\partial \mathbf{u}}{\partial \eta} \cdot \mathbf{t} \\ 0 \\ 0 \\ 0 \end{pmatrix},$$

where the incoming acoustic tangential component is given by:

$$(39) \quad \mathcal{T}_{acou}^- \approx \tilde{\mathcal{T}}_{acou}^- := \beta_l u_t \left[ \frac{\partial p}{\partial \eta} - \rho c \frac{\partial \mathbf{u}}{\partial \eta} \cdot \mathbf{n} \right] + \beta_t \rho c^2 \frac{\partial \mathbf{u}}{\partial \eta} \cdot \mathbf{t}.$$

While the optimal choice of relaxation parameters  $\beta_l, \beta_t$  remains an active area of research [17, 16, 19], in this work, the approach proposed in [33] for low Mach number flows is preferred. In that study, the authors perform a low-Mach asymptotic expansion of the incoming acoustic wave equation and demonstrated that suitable transverse relaxation coefficients for the incoming acoustic wave are given by:

$$(40) \quad \beta = \beta_l = \beta_t = \text{Ma}_\infty.$$

In the viscous setting, reference [13] proposes to impose boundary conditions that enforce vanishing normal derivatives of the normal-tangential component of the deviatoric stress tensor  $\boldsymbol{\tau}$  and vanishing normal derivatives of the normal component of the heat flux  $\mathbf{q}$ , namely,

$$(41) \quad \frac{\partial(\mathbf{t}^T \boldsymbol{\tau} \mathbf{n})}{\partial \xi} = 0, \quad \frac{\partial(\mathbf{q} \cdot \mathbf{n})}{\partial \xi} = 0.$$

2.2.2. *Subsonic inflow.* A subsonic inflow consists of  $d + 1$  incoming characteristics: acoustic, entropy and vorticity waves. Following the rationale applied to outflow boundary conditions, the objective is to approximate

$$(42) \quad \mathcal{L}_{\text{inflow}}^- := \begin{pmatrix} \mathcal{L}_{\text{acou}}^- \\ \mathcal{L}_{\text{entropy}}^- \\ \mathcal{L}_{\text{vorticity}}^- \\ 0 \end{pmatrix} = \begin{pmatrix} (u_n - c) \left[ \frac{\partial p}{\partial \xi} - \rho c \frac{\partial \mathbf{u}}{\partial \xi} \cdot \mathbf{n} \right] \\ u_n \left[ c^2 \frac{\partial \rho}{\partial \xi} - \frac{\partial p}{\partial \xi} \right] \\ u_n \left[ -\frac{\partial \mathbf{u}}{\partial \xi} \cdot \mathbf{t} \right] \\ 0 \end{pmatrix}.$$

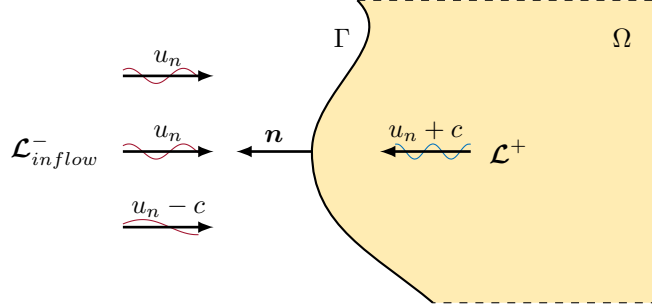


FIGURE 3. Schematic representation of the incoming,  $\mathcal{L}_{\text{inflow}}^-$ , and outgoing,  $\mathcal{L}^+$ , characteristic amplitudes at a subsonic inflow boundary  $\Gamma$ .

A common approach in the finite difference framework is to model the incoming characteristic amplitudes  $\mathcal{L}_{\text{inflow}}^-$  by imposing the target velocity  $\mathbf{u}_\infty$  and the static temperature  $\theta_\infty$ , leading to

$$(43) \quad \mathcal{L}_{\text{inflow}}^- \approx \tilde{\mathcal{L}}_{\text{inflow}}^- = \begin{pmatrix} -D_{u_n} \rho c (\mathbf{u} - \mathbf{u}_\infty) \cdot \mathbf{n} \\ -D_\theta \rho (\theta - \theta_\infty) \\ -D_{u_t} (\mathbf{u} - \mathbf{u}_\infty) \cdot \mathbf{t} \\ 0 \end{pmatrix}, \quad \mathbf{D}^- = \begin{pmatrix} D_{u_n} & 0 & 0 & 0 \\ 0 & D_\theta & 0 & 0 \\ 0 & 0 & D_{u_t} & 0 \\ 0 & 0 & 0 & 0 \end{pmatrix},$$

where the precise definition of the relaxation factors  $D_{u_n}, D_\theta, D_{u_t}$  can be found in [33, A.4]. In this particular case, no modification of the viscous contributions  $\mathcal{V}$  is necessary, since density  $\rho$  and pressure  $p$  are determined by the continuity equation, which excludes any viscous terms [13].

A different approach, discussed in [24, 25], imposes the mass flow rate by specifying the target density  $\rho_\infty$  and the target velocity  $\mathbf{u}_\infty$ , leading to

$$(44) \quad \mathcal{L}_{\text{inflow}}^- \approx \tilde{\mathcal{L}}_{\text{inflow}}^- = \begin{pmatrix} -D_{u_n} \rho c (\mathbf{u} - \mathbf{u}_\infty) \cdot \mathbf{n} \\ D_\rho c^2 (\rho - \rho_\infty) \\ -D_{u_t} (\mathbf{u} - \mathbf{u}_\infty) \cdot \mathbf{t} \\ 0 \end{pmatrix}, \quad \mathbf{D}^- = \begin{pmatrix} D_{u_n} & 0 & 0 & 0 \\ 0 & D_\rho & 0 & 0 \\ 0 & 0 & D_{u_t} & 0 \\ 0 & 0 & 0 & 0 \end{pmatrix},$$

where the relaxation factors  $D_{u_n}, D_\rho, D_{u_t}$  are defined as

$$(45) \quad D_{u_n} = \sigma_u \frac{c(1 - \text{Ma}_\infty^2)}{L}, \quad D_\rho = \sigma_\rho \frac{c}{L}, \quad D_{u_t} = \sigma_t \frac{c}{L},$$

with  $\sigma_u, \sigma_p$  and  $\sigma_t$  being tunable parameters that influence the rate of relaxation towards the target values. In contrast to the previous ansatz, reference [13] proposes an alternative strategy that enforces a vanishing normal derivative of the normal-normal component of the deviatoric stress tensor  $\boldsymbol{\tau}$  at the boundary, namely,

$$(46) \quad \frac{\partial(\mathbf{n}^T \boldsymbol{\tau} \mathbf{n})}{\partial \xi} = 0.$$

This condition ensures that normal stress components do not introduce spurious numerical artifacts at the inflow boundary, particularly in cases where viscosity plays a significant role.

For imposition of conditions on an inflow, including total temperature  $\theta_t$ , total pressure  $p_t$  and flow direction  $\mathbf{u}/\|\mathbf{u}\|$  refer to [25, 18].

The treatment of tangential contributions  $\mathcal{T}^-$  for incoming waves in subsonic inflows remains barely discussed in literature. Typically, these contributions are neglected by setting the tangential relaxation coefficient  $\beta = 0$ .

**2.3. Generalized characteristic relaxation boundary conditions.** In their seminal work [12] from 2013, the authors introduced the concept of Generalized Characteristic Relaxation Boundary Conditions (GRCBCs) within a finite difference (FD) framework. The primary distinction between GRCBCs and the NSCBCs lies in the definition of the relaxation matrix  $\mathbf{D}^-$  in equation (32).

GRCBCs originate from a first-order, one-sided upwind finite difference scheme, where the characteristic length  $L = |\mathbf{x}_b - \mathbf{x}_g|$  represents the distance between a boundary point  $\mathbf{x}_b$  and a ghost point  $\mathbf{x}_g$ . Inside the domain, the CFL condition dictates that, for the maximum propagation speed  $\lambda_{max} = \max\{|u_n + c|, |u_n - c|\}$ , the time step  $\Delta t$  must adhere to the stability constraint

$$\Delta t \lesssim \frac{L_i}{\lambda_{max}}, \quad L_i := |\mathbf{x}_b - \mathbf{x}_i|,$$

where  $\mathbf{x}_i$  is the first interior mesh point. From this consideration, it follows that the length  $L$  must satisfy  $L \geq L_i$  to comply with the CFL condition. The natural choice, therefore, is to set  $L = L_i$ , leading to a relaxation matrix that depends solely on the mesh size, for instance,

$$(47) \quad \mathbf{D}^- := -\frac{1}{L_i} \mathbf{\Lambda}^-.$$

Since the only difference between GRCBCs and NSCBCs lies in the definition of the relaxation matrix  $\mathbf{D}^-$ , other aspects (including the imposition of the transverse relaxation parameter  $\beta$ , the target state  $\mathbf{U}^-$ , and the viscous contributions  $\mathcal{V}$ ) remain unchanged from the NSCBC framework.

It is important to note that, in the finite element (FE) context, the concept of a first interior mesh point  $\mathbf{x}_i$  is inherently ambiguous due to differences in the underlying spatial discretization. Addressing this issue within the FE framework constitutes a key novelty of this work and will be extensively discussed in Section 4.2.

### 3. HYBRIDIZABLE DISCONTINUOUS GALERKIN METHOD FOR COMPRESSIBLE FLOWS

**3.1. Mesh partition and functional spaces.** Consider a partition  $\mathcal{T}_h$  of the domain  $\Omega$  into a shape-regular, uniform and non-overlapping  $d$ -simplices with

$$\max_{T \in \mathcal{T}_h} \frac{h_T^d}{|T|} \leq C \quad C > 0 \quad \forall T \in \mathcal{T}_h, \quad h_T \leq Ch \quad C > 0 \quad \forall T \in \mathcal{T}_h,$$

where  $h_T$  denotes the element diameter, and the global mesh size  $h$  is defined as

$$h_T := \text{diam}(T), \quad h := \max_{T \in \mathcal{T}_h} h_T.$$

Further, let  $\mathcal{F}_h$  denote the set containing the mesh skeleton, which consists of the sets of interior facets  $\mathcal{F}_h^{\text{int}}$  and exterior facets  $\mathcal{F}_h^{\text{ext}}$ , given by

$$\mathcal{F}_h := \bigcup_{T \in \mathcal{T}_h} \partial T, \quad \mathcal{F}_h^{\text{int}} := \mathcal{F}_h \setminus \partial \Omega, \quad \mathcal{F}_h^{\text{ext}} := \mathcal{F}_h \cap \partial \Omega.$$

On a shared interface  $F = \partial T^+ \cap \partial T^- \in \mathcal{F}_h^{\text{int}}$  between two adjacent elements  $T^+$  and  $T^-$  with outward unit normal vectors  $\mathbf{n}^+ = -\mathbf{n}^-$ , let  $\mathbf{V}^\pm$  denote the traces of the restriction of a matrix-valued function  $\mathbf{v}$  onto the respective elements. The jump operator for the traces, see [22, 29], is then defined as

$$\llbracket \mathbf{v} \mathbf{n} \rrbracket := \mathbf{v}^+ \mathbf{n}^+ + \mathbf{v}^- \mathbf{n}^-.$$

Let  $L^2(\Omega)$  denote the space of real-valued square-integrable functions over  $\Omega$ , equipped with the inner product and norm

$$(u, v) := \sum_{T \in \mathcal{T}_h} \int_T uv \, d\mathbf{x}, \quad \|u\| := \sqrt{(u, u)},$$

and define  $L^2(\mathcal{F}_h)$  as the space of real-valued square-integrable functions on  $\mathcal{F}_h$ , with inner product and norm

$$\langle u, v \rangle_{\mathcal{F}_h} := \sum_{F \in \mathcal{F}_h} \int_F uv \, ds, \quad \|u\|_{\mathcal{F}_h} := \sqrt{\langle u, v \rangle_{\mathcal{F}_h}}.$$

For an arbitrary space  $V$ , define  $V(\Omega, \mathbb{R}^n)$  as the vector-valued space, whose  $n$ -components are in  $V$ , and  $V(\Omega, \mathbb{R}^{n \times n})$  as the matrix-valued space, whose  $n^2$ -components are in  $V$ . Then  $L^2(\Omega, \mathbb{R}_{\text{sym}}^{n \times n})$  denotes the space of real-valued square-integrable symmetric tensors over  $\Omega$ , defined as

$$L^2(\Omega, \mathbb{R}_{\text{sym}}^{n \times n}) := \left\{ \mathbf{v} \in L^2(\Omega, \mathbb{R}^{n \times n}) : \mathbf{v} = \mathbf{v}^T \right\}.$$

The spaces of polynomials of degree at most  $k$ , restricted to an element  $T$  or a facet  $F$ , are denoted by  $\mathbb{P}^k(T)$  and  $\mathbb{P}^k(F)$ , respectively. The broken polynomial spaces on  $\mathcal{T}_h$  and  $\mathcal{F}_h$  are then given by:

$$\begin{aligned} \mathbb{P}^k(\mathcal{T}_h) &:= \{v \in L^2(\Omega) : v|_T \in \mathbb{P}^k(T) \forall T \in \mathcal{T}_h\}, \\ \mathbb{P}^k(\mathcal{F}_h) &:= \{v \in L^2(\mathcal{F}_h) : v|_F \in \mathbb{P}^k(F) \forall F \in \mathcal{F}_h\}, \\ \mathbb{P}^k(\mathcal{T}_h, \mathbb{R}^n) &:= \{\mathbf{v} \in L^2(\Omega, \mathbb{R}^n) : \mathbf{v}|_T \in \mathbb{P}^k(T, \mathbb{R}^n) \forall T \in \mathcal{T}_h\}, \\ \mathbb{P}^k(\mathcal{F}_h, \mathbb{R}^n) &:= \{\mathbf{v} \in L^2(\mathcal{F}_h, \mathbb{R}^n) : \mathbf{v}|_F \in \mathbb{P}^k(F, \mathbb{R}^n) \forall F \in \mathcal{F}_h\}, \\ \mathbb{P}^k(\mathcal{T}_h, \mathbb{R}_{\text{sym}}^{n \times n}) &:= \{\mathbf{v} \in L^2(\Omega, \mathbb{R}_{\text{sym}}^{n \times n}) : \mathbf{v}|_T \in \mathbb{P}^k(T, \mathbb{R}_{\text{sym}}^{n \times n}) \forall T \in \mathcal{T}_h\}. \end{aligned}$$

**3.2. Hybridizable Discontinuous Galerkin method.** We consider a recently developed mixed Hybridizable Discontinuous Galerkin method presented in [34], which, in addition to the conservative variables  $\mathbf{U}$ , introduces as mixed variables the rate-of-strain tensor  $\boldsymbol{\varepsilon}$ , see (4), and the temperature gradient  $\boldsymbol{\phi} = \nabla\theta$ . The discrete variational formulation of the compressible Navier-Stokes equations

$$(48) \quad \frac{\partial \mathbf{U}}{\partial t} + \text{div}(\mathbf{F}(\mathbf{U}) - \mathbf{G}(\mathbf{U}, \boldsymbol{\varepsilon}, \boldsymbol{\phi})) = \mathbf{0} \quad \text{in } \Omega \times (0, t_{\text{end}}],$$

is derived by the standard procedure of multiplying by a suitable test function, integrating by parts, and enforcing numerical flux continuity. The resulting formulation reads:

Find  $(\mathbf{U}_h, \widehat{\mathbf{U}}_h, \boldsymbol{\varepsilon}_h, \boldsymbol{\phi}_h) \in U_h \times \widehat{U}_h \times \Xi_h \times \Theta_h$  such that

(49a)

$$\sum_{T \in \mathcal{T}_h} \int_T \frac{\partial \mathbf{U}_h}{\partial t} \cdot \mathbf{V}_h \, d\mathbf{x} - \int_T (\mathbf{F}(\mathbf{U}_h) - \mathbf{G}(\mathbf{U}_h, \boldsymbol{\varepsilon}_h, \boldsymbol{\phi}_h)) : \nabla \mathbf{V}_h \, d\mathbf{x} + \int_{\partial T} (\widehat{\mathbf{F}}_h - \widehat{\mathbf{G}}_h) \mathbf{n} \cdot \mathbf{V}_h \, ds = 0,$$

$$(49b) \quad - \sum_{F \in \mathcal{F}_h^{\text{int}}} \int_F [(\widehat{\mathbf{F}}_h - \widehat{\mathbf{G}}_h) \mathbf{n}] \cdot \widehat{\mathbf{V}}_h \, ds + \sum_{F \in \mathcal{F}_h^{\text{ext}}} \int_F \widehat{\mathbf{F}}_h \cdot \widehat{\mathbf{V}}_h \, ds = 0,$$

$$(49c) \quad \sum_{T \in \mathcal{T}_h} \int_T \boldsymbol{\varepsilon}_h : \boldsymbol{\zeta}_h \, d\mathbf{x} + \int_T \mathbf{u}_h \cdot \text{div}(\boldsymbol{\zeta}_h - \frac{1}{3} \text{tr}(\boldsymbol{\zeta}_h) \mathbf{I}) \, d\mathbf{x} - \int_{\partial T} \widehat{\mathbf{u}}_h \cdot \left[ \boldsymbol{\zeta}_h - \frac{1}{3} \text{tr}(\boldsymbol{\zeta}_h) \mathbf{I} \right] \mathbf{n} \, ds = 0,$$

$$(49d) \quad \sum_{T \in \mathcal{T}_h} \int_T \boldsymbol{\phi}_h \cdot \boldsymbol{\varphi}_h \, d\mathbf{x} + \int_T \theta_h \text{div}(\boldsymbol{\varphi}_h) \, d\mathbf{x} - \int_{\partial T} \widehat{\theta}_h \boldsymbol{\varphi}_h \cdot \mathbf{n} \, ds = 0,$$

for all  $(\mathbf{V}_h, \widehat{\mathbf{V}}_h, \boldsymbol{\zeta}_h, \boldsymbol{\varphi}_h) \in U_h \times \widehat{U}_h \times \Xi_h \times \Theta_h$ , with the discrete spaces chosen as

$$\begin{aligned} U_h &:= L^2((0, t_{\text{end}}]; \mathbb{P}^k(\mathcal{T}_h, \mathbb{R}^4)), & \widehat{U}_h &:= L^2((0, t_{\text{end}}]; \mathbb{P}^k(\mathcal{F}_h, \mathbb{R}^4)), \\ \Xi_h &:= L^2((0, t_{\text{end}}]; \mathbb{P}^k(\mathcal{T}_h, \mathbb{R}_{\text{sym}}^{2 \times 2})), & \Theta_h &:= L^2((0, t_{\text{end}}]; \mathbb{P}^k(\mathcal{T}_h, \mathbb{R}^2)). \end{aligned}$$

To define the discrete velocities  $\mathbf{u}_h := \mathbf{u}(\mathbf{U}_h)$ ,  $\widehat{\mathbf{u}}_h := \mathbf{u}(\widehat{\mathbf{U}}_h)$ , and the discrete temperatures  $\theta_h := \theta(\mathbf{U}_h)$ ,  $\widehat{\theta}_h := \theta(\widehat{\mathbf{U}}_h)$ , we used equation (9). In the formulation,  $\widehat{\mathbf{\Gamma}}_h$  represents the boundary operator, detailed below, imposing the boundary conditions, whereas the numerical fluxes are defined as

$$(50a) \quad \widehat{\mathbf{F}}_h \mathbf{n} := \mathbf{F}(\widehat{\mathbf{U}}_h) \mathbf{n} + \mathbf{S}_c(\mathbf{U}_h - \widehat{\mathbf{U}}_h),$$

$$(50b) \quad \widehat{\mathbf{G}}_h \mathbf{n} := \mathbf{G}(\widehat{\mathbf{U}}_h, \varepsilon_h, \phi_h) \mathbf{n} - \mathbf{S}_d(\mathbf{U}_h - \widehat{\mathbf{U}}_h),$$

where  $\mathbf{S}_c, \mathbf{S}_d$  are convective and viscous stabilization matrices, respectively, chosen to ensure the correct physical behavior of the flow. A detailed discussion on suitable stabilization matrices and their connection to Riemann solvers can be found in [34, 35, 26], whereas the specific expressions employed in this study are detailed in Section 5.

*Remark 3.1.* Following the discussion in [34, 36], the symmetry of the discrete rate-of-strain tensor  $\varepsilon_h = \varepsilon_h^T$  is enforced strongly by properly rearranging the unique off-diagonal components using Voigt notation. For instance in two dimensions, this approach decreases the number of components in the matrix-valued space  $\Xi_h$  from four to three, thereby significantly reducing the computational cost.

**3.3. Boundary conditions and stability considerations.** In HDG methods boundary conditions are imposed weakly via the boundary operator  $\widehat{\mathbf{\Gamma}}_h$  in (49b). Common boundary conditions include:

$$(51a) \quad (\text{Adiabatic wall}) \quad \widehat{\mathbf{\Gamma}}_h = \widehat{\mathbf{\Gamma}}_{ad} := \begin{pmatrix} \widehat{\rho}_h - \rho_h \\ \widehat{\rho} \mathbf{u}_h \\ 1/(\text{Re}_\infty \text{Pr}_\infty) \phi_h \cdot \mathbf{n} \end{pmatrix} - \mathbf{S}_d \begin{pmatrix} 0 \\ \mathbf{0} \\ \rho E_h - \rho \widehat{E}_h \end{pmatrix},$$

$$(51b) \quad (\text{Isothermal wall}) \quad \widehat{\mathbf{\Gamma}}_h = \widehat{\mathbf{\Gamma}}_{iso} := \widehat{\mathbf{U}}_h - \begin{pmatrix} \rho_h \\ \mathbf{0} \\ \rho_h \theta_{\text{wall}} / \gamma \end{pmatrix},$$

$$(51c) \quad (\text{Inviscid wall}) \quad \widehat{\mathbf{\Gamma}}_h = \widehat{\mathbf{\Gamma}}_{inv} := \widehat{\mathbf{U}}_h - \begin{pmatrix} \rho_h \\ (\mathbf{I} - \mathbf{n} \otimes \mathbf{n}) \rho \mathbf{u}_h \\ \rho E_h \end{pmatrix}.$$

In addition, in aerodynamics, it is common to impose the static pressure on a subsonic outflow boundary by setting

$$(52) \quad \widehat{\mathbf{\Gamma}}_h = \widehat{\mathbf{\Gamma}}_{p_\infty} := \widehat{\mathbf{U}}_h - \mathbf{U}_{p_\infty},$$

where the pressure target state  $\mathbf{U}_{p_\infty}$  is defined as

$$(53) \quad \mathbf{U}_{p_\infty} := \begin{pmatrix} \rho_h \\ \rho \mathbf{u}_h \\ p_\infty / (\gamma - 1) + \rho_h |\mathbf{u}_h|^2 / 2 \end{pmatrix}.$$

This boundary condition is particularly effective in the wake of a body, as it allows entropy waves and vorticity waves to leave the domain. However, it has a significant drawback: it causes the full outgoing acoustic wave to be reflected back into the domain, as the imposed target pressure  $p_\infty$  acts as a hard boundary for pressure waves.

A more suitable boundary condition for compressible flow, commonly referred to as the far-field boundary condition [34, 27, 26], uses a characteristic approach

$$(54) \quad \widehat{\mathbf{\Gamma}}_h = \widehat{\mathbf{\Gamma}}_\infty := \widehat{\mathbf{A}}^+(\widehat{\mathbf{U}}_h - \mathbf{U}_h) - \widehat{\mathbf{A}}^-(\widehat{\mathbf{U}}_h - \mathbf{U}_\infty),$$

where the far-field target state  $\mathbf{U}_\infty$  is given by

$$(55) \quad \mathbf{U}_\infty := \begin{pmatrix} \rho_\infty \\ \rho_\infty \mathbf{u}_\infty \\ \rho_\infty E_\infty \end{pmatrix}.$$

Here,  $\hat{\mathbf{A}}$  is the convective Jacobian, as defined in (13a), evaluated at the intermediate state  $\widehat{\mathbf{U}}_h$ . The incoming and outgoing convective Jacobians, denoted by  $\hat{\mathbf{A}}^\mp$ , are obtained via the decomposition of  $\hat{\mathbf{A}}$  evaluated at the intermediate state  $\widehat{\mathbf{U}}_h$  into its characteristic wave contributions, as given in (15). This decomposition into incoming and outgoing contributions, based on the Jacobians  $\hat{\mathbf{A}}^\mp$ , ensures an upwind discretization, as it correctly determines the wave propagation direction that is used to determine the intermediate state  $\widehat{\mathbf{U}}_h$ . Specifically, outgoing waves,  $\hat{\mathbf{A}}^+(\widehat{\mathbf{U}}_h - \mathbf{U}_h)$ , are determined based on the interior state  $\mathbf{U}_h$ , while incoming waves,  $\hat{\mathbf{A}}^-(\widehat{\mathbf{U}}_h - \mathbf{U}_\infty)$ , are determined based on the exterior state  $\mathbf{U}_\infty$ .

In supersonic flows, where information cannot propagate upstream, the specified boundary condition ensures the correct physical behavior. Specifically, in an outflow scenario,  $\hat{\mathbf{A}}^- = \mathbf{0}$ , meaning only outgoing characteristics are considered. In an inflow scenario,  $\hat{\mathbf{A}}^+ = \mathbf{0}$ , ensuring that only the upstream state influences the intermediate state  $\widehat{\mathbf{U}}_h$ .

For subsonic flows, the far-field boundary operator (54) effectively absorbs planar acoustic waves, but significant reflection may occur when oblique waves and vortices cross the boundary, as observed in the numerical experiments in Section 5.

A limitation of the formulation in (54) arises when the boundary is aligned in flow direction, i.e.  $u_n = 0$ , as the convective Jacobian  $\hat{\mathbf{A}}$  then has  $d$  zero eigenvalues. This might lead to difficulties when solving the system, e.g. when using an iterative solver. A practical workaround has been described in [34] by introducing a threshold  $\varepsilon \ll 1$ , such that

$$\tilde{\lambda}_i^+ = \max(\lambda_i^+, \varepsilon), \quad \tilde{\lambda}_i^- = \min(\lambda_i^-, -\varepsilon).$$

Ensuring that the convective Jacobian  $\hat{\mathbf{A}}$  has non-zero eigenvalues, we propose a numerically more stable discretization by premultiplying (54) by the inverse of the absolute convective Jacobian  $|\hat{\mathbf{A}}|^{-1} = \hat{\mathbf{P}}|\hat{\boldsymbol{\Lambda}}|^{-1}\hat{\mathbf{P}}^{-1}$ , where the hat on all matrices is to recall that they are computed at the intermediate state  $\widehat{\mathbf{U}}_h$ . This results in the modified boundary condition:

$$|\hat{\mathbf{A}}|^{-1} \left[ \hat{\mathbf{A}}^+(\widehat{\mathbf{U}}_h - \mathbf{U}_h) - \hat{\mathbf{A}}^-(\widehat{\mathbf{U}}_h - \mathbf{U}_\infty) \right] = |\hat{\mathbf{A}}|^{-1}(\hat{\mathbf{A}}^+ - \hat{\mathbf{A}}^-)\widehat{\mathbf{U}}_h - |\hat{\mathbf{A}}|^{-1}\hat{\mathbf{A}}^+\mathbf{U}_h + |\hat{\mathbf{A}}|^{-1}\hat{\mathbf{A}}^-\mathbf{U}_\infty.$$

Since  $\hat{\mathbf{A}}^+ - \hat{\mathbf{A}}^- = |\hat{\mathbf{A}}|$ , this simplifies to

$$\widehat{\mathbf{U}}_h - |\hat{\mathbf{A}}|^{-1}\hat{\mathbf{A}}^+\mathbf{U}_h + |\hat{\mathbf{A}}|^{-1}\hat{\mathbf{A}}^-\mathbf{U}_\infty = \mathbf{0}.$$

From the definitions in (16), we identify  $\hat{\mathbf{Q}}^+ = |\hat{\mathbf{A}}|^{-1}\hat{\mathbf{A}}^+$  and  $\hat{\mathbf{Q}}^- = -|\hat{\mathbf{A}}|^{-1}\hat{\mathbf{A}}^-$ . Then, the final stabilized boundary operator is expressed as

$$(56) \quad \hat{\mathbf{\Gamma}}_h = \hat{\mathbf{\Gamma}}_\infty^{\mathcal{Q}} := \widehat{\mathbf{U}}_h - \hat{\mathbf{Q}}^+\mathbf{U}_h - \hat{\mathbf{Q}}^-\mathbf{U}_\infty = \widehat{\mathbf{U}}_h - \frac{\mathbf{U}_h + \mathbf{U}_\infty}{2} - \hat{\mathbf{P}}\hat{\mathbf{I}}_n\hat{\mathbf{P}}^{-1}\frac{\mathbf{U}_h - \mathbf{U}_\infty}{2}.$$

*Remark 3.2.* Assuming  $\hat{\mathbf{Q}}^+$  and  $\hat{\mathbf{Q}}^-$  are constant, then (56) resembles the solution of a linear hyperbolic problem with constant coefficients.

*Remark 3.3.* In the case of a singular vanishing eigenvalue  $\lambda_i = 0$ , the matrix  $\hat{\mathbf{I}}_n$  has a zero diagonal entry, and (56) simplifies to averaging between the two states  $\mathbf{U}_h$  and  $\mathbf{U}_\infty$  for the corresponding wave, analogously to the Lax-Friedrichs flux [34]. The same holds true for multiple vanishing eigenvalues.

#### 4. CHARACTERISTIC BOUNDARY CONDITIONS FOR HYBRIDIZABLE DISCONTINUOUS GALERKIN METHOD

In this work we devise for the first time the Navier-Stokes characteristic boundary conditions (NSCBCs) of Subsection 2.2 and the generalized characteristic relaxation boundary conditions (GRCBCs) of Subsection 2.3 in a Hybridizable Discontinuous Galerkin (HDG) setting.

To simplify the explanation of the implementation, we initially consider the one-dimensional, inviscid case (33) in conservative form, thus

$$(57) \quad \mathbf{P} \left( \frac{\partial \mathbf{W}}{\partial t} + \mathcal{L}^- + \mathcal{L}^+ \right) = \frac{\partial \mathbf{U}}{\partial t} + \mathbf{P} \mathcal{L}^- + \mathbf{P} \mathcal{L}^+ = \mathbf{0} \quad \text{on} \quad \partial \Omega \times (0, t_{end}],$$

while the extension to the multidimensional viscous setting is addressed subsequently.

For ease of notation, every scalar, vector or matrix evaluated at the intermediate state  $\widehat{\mathbf{U}}_h$  is denoted by a hat symbol, e.g. the eigenvectors  $\widehat{\mathbf{P}}$ .

We begin by discretizing equation (57) at the boundary  $\partial \Omega$  using an implicit Euler method considering a time step  $\Delta t$  on a time interval  $0 = t_0 < t_n < \dots \leq t_{end}$  with  $t_n := n\Delta t$ . Then the discrete system of equations reads as

$$(58) \quad \frac{\widehat{\mathbf{U}}_h^{n+1} - \widehat{\mathbf{U}}_h^n}{\Delta t} + \widehat{\mathbf{P}}^{n+1} \widehat{\mathcal{L}}^{n+1,-} + \widehat{\mathbf{P}}^{n+1} \widehat{\mathcal{L}}^{n+1,+} = \mathbf{0},$$

where the superscript  $n \in \{0, 1, \dots\}$  refers to an evaluation at time  $t_n$ . Unless otherwise stated, we omit the superscript  $n + 1$ , referring to the time evaluation  $t_{n+1}$ , for the remainder of this section.

*Remark 4.1.* The choice of time marching scheme is not restricted to an implicit Euler, but has been chosen for sake of simplicity in the derivation. We recommend using the same time marching scheme as for the elementwise conservative variable  $\mathbf{U}_h$  in (49a).

We rearrange terms by multiplying with the denominator of the time marching scheme i.e.  $\Delta t$ , leading to

$$(59) \quad \widehat{\mathbf{U}}_h - \widehat{\mathbf{U}}_h^n + \Delta t \widehat{\mathbf{P}} \widehat{\mathcal{L}}^- + \Delta t \widehat{\mathbf{P}} \widehat{\mathcal{L}}^+ = \mathbf{0}.$$

By mimicking the filter from (54), outgoing waves can be simply determined by  $\widehat{\mathbf{A}}^+(\widehat{\mathbf{U}}_h - \mathbf{U}_h)$ , whereas we aim to model incoming waves to achieve better accuracy. Therefore, we premultiply (59) by the incoming Jacobian  $\widehat{\mathbf{A}}^-$ , resulting in

$$(60) \quad \widehat{\mathbf{A}}^- \left( \widehat{\mathbf{U}}_h - \widehat{\mathbf{U}}_h^n \right) + \Delta t \widehat{\mathbf{A}}^- \widehat{\mathbf{P}} \widehat{\mathcal{L}}^- + \Delta t \widehat{\mathbf{A}}^- \widehat{\mathbf{P}} \widehat{\mathcal{L}}^+ = \mathbf{0}.$$

On the one hand, we observe that outgoing characteristic amplitudes  $\widehat{\mathcal{L}}^+$ , see (27a), vanish, since

$$(61) \quad \widehat{\mathbf{A}}^- \widehat{\mathbf{P}} \widehat{\mathcal{L}}^+ = \widehat{\mathbf{P}} \widehat{\Lambda}^- \widehat{\Lambda}^+ \widehat{\mathbf{P}}^{-1} \frac{\partial \mathbf{U}_h}{\partial \xi} = \mathbf{0},$$

due to the property  $\widehat{\Lambda}^- \widehat{\Lambda}^+ = \mathbf{0}$  of the incoming and outgoing eigenvalues. On the other hand, the incoming characteristic amplitudes  $\widehat{\mathcal{L}}^-$  can be expressed by the full set of characteristic amplitudes  $\widehat{\mathcal{L}}$ , since the following identity holds

$$(62) \quad \widehat{\mathbf{A}}^- \widehat{\mathbf{P}} \widehat{\mathcal{L}}^- = \widehat{\mathbf{P}} \widehat{\Lambda}^- \widehat{\mathcal{L}}^- = \widehat{\mathbf{P}} \widehat{\Lambda}^- \widehat{\mathcal{L}} = \widehat{\mathbf{A}}^- \widehat{\mathbf{P}} \widehat{\mathcal{L}}.$$

Therefore, the system of equations (60) filters outgoing waves, while incoming waves are retained.

Using (61) and (62) we rewrite the system as

$$(63) \quad \widehat{\mathbf{A}}^- \left( \widehat{\mathbf{U}}_h - \widehat{\mathbf{U}}_h^n + \Delta t \widehat{\mathbf{P}} \widehat{\mathcal{L}} \right) = \mathbf{0},$$

and in the spirit of (31), we model the full set of characteristic amplitudes

$$(64) \quad \widehat{\mathcal{L}} \approx \widetilde{\widehat{\mathcal{L}}} := \widehat{\mathbf{D}} \widehat{\mathbf{P}}^{-1} \left( \widehat{\mathbf{U}}_h - \mathbf{U}^- \right), \quad \widehat{\mathbf{D}} \sim -\frac{\widehat{\Lambda}}{L},$$

since the correct incoming characteristic amplitudes are selected based on the eigenvalues of the incoming Jacobian  $\widehat{\mathbf{A}}^-$ . This behavior can be particularly advantageous at boundaries where flow inversion occurs, as the number of incoming characteristic amplitudes either increases or decreases, depending on whether the boundary transitions to a subsonic inflow or outflow condition, respectively.

Inserting definition (64) of the modeled characteristic amplitudes  $\tilde{\mathcal{L}}$  into (63), yields

$$(65) \quad \hat{\mathbf{A}}^- \left( \hat{\mathbf{U}}_h - \hat{\mathbf{U}}_h^n + \Delta t \hat{\mathbf{P}} \hat{\mathbf{D}} \hat{\mathbf{P}}^{-1} \left( \hat{\mathbf{U}}_h - \mathbf{U}^- \right) \right) = \mathbf{0}.$$

Ultimately, we couple the above expression with the outgoing waves  $\hat{\mathbf{A}}^+(\hat{\mathbf{U}}_h - \mathbf{U}_h)$ , and define the characteristic boundary operator  $\hat{\Gamma}_C$  by combining equation (65), resulting in

$$(66) \quad \hat{\Gamma}_h = \hat{\Gamma}_C := \underbrace{\hat{\mathbf{A}}^+(\hat{\mathbf{U}}_h - \mathbf{U}_h)}_{\text{outgoing}} - \underbrace{\hat{\mathbf{A}}^- \left( \hat{\mathbf{U}}_h - \hat{\mathbf{U}}_h^n + \Delta t \hat{\mathbf{P}} \hat{\mathbf{D}} \hat{\mathbf{P}}^{-1} \left( \hat{\mathbf{U}}_h - \mathbf{U}^- \right) \right)}_{\text{incoming}}.$$

Note that the resulting characteristic boundary operator (66) resembles the far-field operator (54), with a modified exterior state modeling the non-reflecting behavior.

Alternatively, following the same procedure as for the modified far-field operator (56), we can express the characteristic boundary operator (66) in a more stable variant

$$(67) \quad \hat{\Gamma}_h = \hat{\Gamma}_C^Q := \hat{\mathbf{U}}_h - \hat{\mathbf{Q}}^+ \mathbf{U}_h - \hat{\mathbf{Q}}^- \left[ \hat{\mathbf{U}}_h^n - \Delta t \hat{\mathbf{P}} \hat{\mathbf{D}} \hat{\mathbf{P}}^{-1} \left( \hat{\mathbf{U}}_h - \mathbf{U}^- \right) \right].$$

**4.1. Implementation of the Navier-Stokes characteristic boundary conditions.** With the definition of characteristic boundary operator  $\hat{\Gamma}_C$  in (66), the Navier-Stokes characteristic boundary conditions from Subsection 2.2 are immediately recovered by appropriately choosing the relaxation matrix  $\hat{\mathbf{D}}$  and the target state  $\mathbf{U}^-$ .

**4.1.1. Subsonic outflow.** The incoming acoustic wave on a subsonic outflow is modeled by imposing the target pressure  $p_\infty$  as in (35), namely,

$$(68) \quad \hat{\mathbf{D}} = \begin{pmatrix} \hat{D}_p & 0 & 0 & 0 \\ 0 & -\hat{u}_n & 0 & 0 \\ 0 & 0 & -\hat{u}_n & 0 \\ 0 & 0 & 0 & -(\hat{u}_n + \hat{c}) \end{pmatrix}, \quad \mathbf{U}^- = \mathbf{U}_{p_\infty} := \begin{pmatrix} p_\infty \\ \rho \mathbf{u}_h \\ p_\infty / (\gamma - 1) + \rho_h |\mathbf{u}_h|^2 / 2 \end{pmatrix}.$$

**4.1.2. Subsonic inflow.** For a subsonic inflow the incoming characteristic amplitudes can be modeled by either imposing the target density  $\rho_\infty$  and the target velocity  $\mathbf{u}_\infty$  as in (44), yielding

$$(69) \quad \hat{\mathbf{D}} = \begin{pmatrix} \hat{D}_{u_n} & 0 & 0 & 0 \\ 0 & \hat{D}_\rho & 0 & 0 \\ 0 & 0 & \hat{D}_{u_t} & 0 \\ 0 & 0 & 0 & -(\hat{u}_n + \hat{c}) \end{pmatrix}, \quad \mathbf{U}^- = \mathbf{U}_{\rho \mathbf{u}_\infty} := \begin{pmatrix} \rho_\infty \\ \rho \mathbf{u}_\infty \\ p_h / (\gamma - 1) + \rho_\infty |\mathbf{u}_\infty|^2 / 2 \end{pmatrix},$$

or by imposing the target density  $\rho_\infty$ , the target velocity  $\mathbf{u}_\infty$  and the target temperature  $\theta_\infty$  as in (43), that is

$$(70) \quad \hat{\mathbf{D}} = \begin{pmatrix} \hat{D}_{u_n} & 0 & 0 & 0 \\ 0 & \hat{D}_\theta & 0 & 0 \\ 0 & 0 & \hat{D}_{u_t} & 0 \\ 0 & 0 & 0 & -(\hat{u}_n + \hat{c}) \end{pmatrix}, \quad \mathbf{U}^- = \mathbf{U}_{\theta_\infty} := \rho(\theta_h) \begin{pmatrix} 1 \\ \mathbf{u}_\infty \\ \theta_h / \gamma + |\mathbf{u}_\infty|^2 / 2 \end{pmatrix},$$

where the density,  $\rho(\theta_h)$ , has been derived under the assumption of isentropic flow conditions

$$(71) \quad \rho(\theta_h) = \rho_\infty \left( \frac{\theta_h}{\theta_\infty} \right)^{\frac{1}{\gamma-1}}.$$

**4.2. Implementation of the generalized characteristic relaxation boundary conditions.** Extending the concept of generalized relaxation boundary conditions (GRCBCs) from Subsection 2.3 in a finite element framework is more challenging due to the ambiguous definition of the first inner mesh point  $\mathbf{x}_i$  to the boundary, required to determine the characteristic length  $L_i$  in the solely mesh-dependent relaxation matrix  $\hat{\mathbf{D}}$ , see (47). Numerical experiments conducted with element local diameter  $L_i = h_T$  and  $L_i = h_T / (k + 1)$  consistently resulted in a hard boundary.

To address this issue, we propose a novel approach. Following the rationale of [12], any characteristic wave should fulfill a CFL condition to prevent stiffness in the numerical approximation, i.e., in matrix notation,

$$(72) \quad \Delta t \mathbf{L}^{-1} |\widehat{\mathbf{\Lambda}}| \leq \mathbf{C}, \quad \mathbf{0} < \mathbf{C} \leq \mathbf{I},$$

where  $\mathbf{L}$  and  $\mathbf{C}$  are diagonal matrices and the symbols  $<, \leq$  should be understood to act component-wise on the diagonal.

Let  $\mathbf{L}$  be a matrix of different characteristic lengths. Assuming a given CFL-matrix  $\mathbf{C}$  and comparing (72) with (64), we can define the relaxation matrix  $\widehat{\mathbf{D}}$  as

$$(73) \quad \widehat{\mathbf{D}} := \frac{1}{\Delta t} \mathbf{C} = \frac{1}{\Delta t} \begin{pmatrix} C_0 & 0 & 0 & 0 \\ 0 & C_1 & 0 & 0 \\ 0 & 0 & C_2 & 0 \\ 0 & 0 & 0 & C_3 \end{pmatrix}.$$

The emerging relaxation matrix  $\widehat{\mathbf{D}}$  can be interpreted as if the first-order, one-sided upwind finite difference scheme from (30) is performed at the characteristic level for different characteristic lengths  $\mathbf{L}$ , instead of a fixed length  $L$ , leading to

$$(74) \quad \frac{\partial \mathbf{W}}{\partial \xi} \stackrel{\text{FD approx.}}{\approx} -\mathbf{L}^{-1} \widehat{\mathbf{P}}^{-1} (\widehat{\mathbf{U}}_h - \mathbf{U}^-).$$

By assuming the characteristic lengths  $\mathbf{L}$  to be equal to

$$\mathbf{L}^{-1} = \frac{1}{\Delta t} \mathbf{C} |\widehat{\mathbf{\Lambda}}|^{-1},$$

and inserting (74) into the definition of the characteristic amplitudes (26a), we recover the modeled characteristic amplitudes  $\widetilde{\mathcal{L}}$  from (64)

$$(75) \quad \widehat{\mathcal{L}} \approx \widetilde{\mathcal{L}} = \frac{1}{\Delta t} \mathbf{C} \widehat{\mathbf{P}}^{-1} (\widehat{\mathbf{U}}_h - \mathbf{U}^-) = \widehat{\mathbf{D}} \widehat{\mathbf{P}}^{-1} (\widehat{\mathbf{U}}_h - \mathbf{U}^-).$$

In the derivation of (75) we exploited the fact, that due to the filtering property of the incoming Jacobian  $\widehat{\mathbf{A}}^-$  in (62), it holds

$$(76) \quad -\widehat{\mathbf{A}}^- \widehat{\mathbf{P}} \widehat{\mathbf{\Lambda}} |\widehat{\mathbf{\Lambda}}|^{-1} \frac{1}{\Delta t} \mathbf{C} = -\widehat{\mathbf{P}} \widehat{\mathbf{\Lambda}}^- \widehat{\mathbf{\Lambda}} |\widehat{\mathbf{\Lambda}}|^{-1} \frac{1}{\Delta t} \mathbf{C} = \widehat{\mathbf{P}} \widehat{\mathbf{\Lambda}}^- \frac{1}{\Delta t} \mathbf{C} = \widehat{\mathbf{A}}^- \widehat{\mathbf{P}} \frac{1}{\Delta t} \mathbf{C},$$

hence we can omit the term  $-\widehat{\mathbf{\Lambda}} |\widehat{\mathbf{\Lambda}}|^{-1}$ .

In comparison to the solely mesh-dependent relaxation matrix  $\widehat{\mathbf{D}}$  described in Subsection 2.3, the proposed method requires the user to specify the CFL-like relaxation factors  $0 < C_i \leq 1$ , for each incoming characteristic wave. To facilitate the choice of relaxation factors  $C_i$ , we provide a prediction on the lower and upper bounds:

- **No relaxation  $\mathbf{C} \rightarrow \mathbf{0}$ :**

On the one hand, the lack of a relaxation matrix  $\widehat{\mathbf{D}}$  leads to a perfectly non-reflecting boundary for planar waves, as will be seen in the numerical experiments. On the other hand, as outlined in Subsection 2.2.1, it may lead to a drift from the target state  $\mathbf{U}^-$ .

- **Full relaxation  $\mathbf{C} \rightarrow \mathbf{I}$**

In this scenario, the contributions of the incoming characteristic amplitudes are fully retained and have the same order of magnitude as the outgoing characteristic amplitudes, allowing the target state  $\mathbf{U}^-$  to be reached more quickly. However, depending on the target state  $\mathbf{U}^-$ , this can result in a highly reflecting boundary condition.

This approach recovers the common HDG boundary conditions, such as the subsonic outflow (52) and the far-field condition (54), as special cases. Assume  $\widehat{\mathbf{D}} = \frac{1}{\Delta t} \mathbf{I}$ , then the boundary operator (66) reduces to

$$\widehat{\mathbf{\Gamma}}_h = \widehat{\mathbf{A}}^+ (\widehat{\mathbf{U}}_h - \mathbf{U}_h) - \widehat{\mathbf{A}}^- (2\widehat{\mathbf{U}}_h - \widehat{\mathbf{U}}_h^n - \mathbf{U}^-),$$

which for  $\widehat{\mathbf{U}}_h^{n+1} \approx \widehat{\mathbf{U}}_h^n$  and target state  $\mathbf{U}^- = \mathbf{U}_\infty$  resembles the far-field operator in (54).

The choice of the CFL factors  $C_i$  can be seen as a trade-off between the two extremes of no relaxation and full relaxation, where the improvement lies in the fact that the user can now adjust the relaxation factors  $C_i$  to the specific problem at hand, allowing for a more flexible boundary condition. Further, the inclusion of additional tangential and viscous contributions is possible and has a significant impact on the numerical solution, as demonstrated in the forthcoming numerical experiments.

**4.3. Multidimensional and viscous setting.** The extension to the complete Navier-Stokes equations follows the same line of thought. On the boundary, we discretize the conservative system of equations (29) by

$$(77) \quad \frac{\widehat{U}_h - \widehat{U}_h^n}{\Delta t} + \widehat{P}\widehat{\mathcal{L}}^- + \widehat{P}\widehat{\mathcal{L}}^+ + \beta\widehat{P}\widehat{\mathcal{T}}^- + \widehat{P}\widehat{\mathcal{T}}^+ - \boldsymbol{\nu} = \mathbf{0}.$$

We rearrange terms and filter the equations by the incoming Jacobian  $\widehat{A}^-$ , yielding

$$(78) \quad \widehat{A}^- \left( \widehat{U}_h - \widehat{U}_h^n \right) + \Delta t \left[ \widehat{A}^- \widehat{P}\widehat{\mathcal{L}}^- + \widehat{A}^- \widehat{P}\widehat{\mathcal{L}}^+ + \beta\widehat{A}^- \widehat{P}\widehat{\mathcal{T}}^- + \widehat{A}^- \widehat{P}\widehat{\mathcal{T}}^+ - \widehat{A}^- \boldsymbol{\nu} \right] = \mathbf{0}.$$

Similarly to the one-dimensional inviscid setting, we observe that outgoing tangential contributions  $\widehat{\mathcal{T}}^+$  vanish, while incoming contributions  $\widehat{\mathcal{T}}^-$  are retained, i.e.

$$\widehat{A}^- \widehat{P}\widehat{\mathcal{T}}^+ = \widehat{A}^- \widehat{Q}^+ \widehat{B} \frac{\partial U^-}{\partial \eta} = \mathbf{0}, \quad \widehat{A}^- \widehat{P}\widehat{\mathcal{T}}^- = \widehat{A}^- \widehat{Q}^- \widehat{B} \frac{\partial U^-}{\partial \eta} = \widehat{A}^- \widehat{B} \frac{\partial U^-}{\partial \eta} = \widehat{A}^- \widehat{P}\widehat{\mathcal{T}},$$

hence we rewrite the system of equations (78) as

$$(79) \quad \widehat{A}^- \left( \widehat{U}_h - \widehat{U}_h^n + \Delta t \left[ \widehat{P}\widehat{\mathcal{L}} + \beta\widehat{P}\widehat{\mathcal{T}} - \boldsymbol{\nu} \right] \right) = \mathbf{0}.$$

We insert the modeled characteristic amplitudes (64) and the conservative definition of the transverse contributions  $\widehat{P}\widehat{\mathcal{T}}$ , to get

$$(80) \quad \widehat{A}^- \left( \widehat{U}_h - \widehat{U}_h^n + \Delta t \left[ \widehat{P}\widehat{D}\widehat{P}^{-1} \left( \widehat{U}_h - U^- \right) + \beta\widehat{B} \frac{\partial U^-}{\partial \eta} - \boldsymbol{\nu} \right] \right) = \mathbf{0}.$$

Ultimately, the definition of the boundary operator (66) remains unchanged, aside from the inclusion of additional tangential and viscous contributions

$$(81) \quad \widehat{\Gamma}_h = \widehat{\Gamma}_c^{\mathcal{T}\boldsymbol{\nu}} := \underbrace{\widehat{A}^+ \left( \widehat{U}_h - U_h \right)}_{\text{outgoing}} - \underbrace{\widehat{A}^- \left( \widehat{U}_h - \widehat{U}_h^n + \Delta t \left[ \widehat{P}\widehat{D}\widehat{P}^{-1} \left( \widehat{U}_h - U^- \right) + \beta\widehat{B} \frac{\partial U^-}{\partial \eta} - \boldsymbol{\nu} \right] \right)}_{\text{incoming}}.$$

**4.3.1. Treatment of the tangential convective contributions  $\mathcal{T}$ .** Unlike the normal derivative, the tangential derivative along the boundary of the facet variable  $\widehat{U}_h$  is defined, and therefore we discretize the tangential contributions as

$$(82) \quad \widehat{B} \frac{\partial U^-}{\partial \eta} := \widehat{B} \frac{\partial \widehat{U}_h}{\partial \eta}.$$

**4.3.2. Treatment of the viscous contributions  $\boldsymbol{\nu}$ .** For the implementation of the viscous contributions  $\boldsymbol{\nu}$ , we exploit the fact that in our discretization the viscous flux  $\mathbf{G}(\mathbf{U}, \boldsymbol{\varepsilon}, \boldsymbol{\phi})$  is linear in the conservative variables  $\mathbf{U}$ , the rate-of-strain tensor  $\boldsymbol{\varepsilon}$  and the temperature gradient  $\boldsymbol{\phi}$ , see equation (3). By regrouping the components of the rate-of-strain tensor  $\boldsymbol{\varepsilon}$  and the components of the temperature gradient  $\boldsymbol{\phi}$  in a Voigt-like form

$$\boldsymbol{\chi} := (\varepsilon_{xx}, \varepsilon_{xy}, \varepsilon_{yy}, \phi_x, \phi_y)^T,$$

we can express  $\boldsymbol{\nu}$  in quasi-linear form as

$$(83) \quad \boldsymbol{\nu} = \frac{\partial(\mathbf{G}\mathbf{n})}{\partial \xi} + \frac{\partial(\mathbf{G}\mathbf{t})}{\partial \eta} = \frac{1}{\text{Re}_\infty} \left[ \mathbf{A}_n^U \frac{\partial \mathbf{U}}{\partial \xi} + \mathbf{A}_n^\chi \frac{\partial \boldsymbol{\chi}}{\partial \xi} + \mathbf{A}_t^U \frac{\partial \mathbf{U}}{\partial \eta} + \mathbf{A}_t^\chi \frac{\partial \boldsymbol{\chi}}{\partial \eta} \right].$$

The viscous Jacobians in (83) are given as

$$(84a) \quad \mathbf{A}_n^U := \frac{\partial(\mathbf{Gn})}{\partial \mathbf{U}}, \quad \mathbf{A}_n^\chi := \frac{\partial(\mathbf{Gn})}{\partial \chi},$$

$$(84b) \quad \mathbf{A}_t^U := \frac{\partial(\mathbf{Gt})}{\partial \mathbf{U}}, \quad \mathbf{A}_t^\chi := \frac{\partial(\mathbf{Gt})}{\partial \chi},$$

where for an arbitrary unit vector  $\mathbf{r} = [r_x, r_y]^\top$  it holds

$$\mathbf{A}_r^U := \frac{\partial(\mathbf{Gr})}{\partial \mathbf{U}} = \frac{2}{\rho} \begin{pmatrix} 0 & 0 & 0 & 0 \\ 0 & 0 & 0 & 0 \\ 0 & 0 & 0 & 0 \\ -\mathbf{r}^\top \boldsymbol{\varepsilon} \mathbf{u} \cdot & \varepsilon_{xx} r_x + \varepsilon_{xy} r_y & \varepsilon_{xy} r_x + \varepsilon_{yy} r_y & 0 \end{pmatrix},$$

$$\mathbf{A}_r^\chi := \frac{\partial(\mathbf{Gr})}{\partial \chi} = \begin{pmatrix} 0 & 0 & 0 & 0 & 0 \\ 2r_x & 2r_y & 0 & 0 & 0 \\ 0 & 2r_x & 2r_y & 0 & 0 \\ 2r_x u_x & 2r_x u_y + 2r_y u_x & 2r_y u_y & \frac{r_x}{\text{Pr}_\infty} & \frac{r_y}{\text{Pr}_\infty} \end{pmatrix}.$$

In order to modify the viscous contributions  $\mathbf{V}$  to accommodate zero-normal gradient viscous conditions as described in Subsection 2.2, we reformulate  $\partial_\xi \chi$  in terms of normal-normal, normal-tangential and tangential-tangential components. Together with the constant rotation matrix  $\mathbf{R}$ , emerging from the assumption of a local orthogonal basis, we express these as

$$(85) \quad \mathbf{R} := \begin{pmatrix} n_x & t_x \\ n_y & t_y \end{pmatrix}, \quad \begin{pmatrix} \varepsilon_{nn} & \varepsilon_{nt} \\ \varepsilon_{nt} & \varepsilon_{tt} \end{pmatrix} = \mathbf{R}^\top \boldsymbol{\varepsilon} \mathbf{R}, \quad \begin{pmatrix} \phi_n \\ \phi_t \end{pmatrix} = \mathbf{R}^\top \boldsymbol{\phi}.$$

Therefore, by rearranging terms we can express the Cartesian derivatives in terms of normal-normal, normal-tangential and tangential-tangential derivatives, namely,

$$(86) \quad \begin{pmatrix} \frac{\partial \varepsilon_{xx}}{\partial \xi} & \frac{\partial \varepsilon_{xy}}{\partial \xi} \\ \frac{\partial \varepsilon_{xy}}{\partial \xi} & \frac{\partial \varepsilon_{yy}}{\partial \xi} \end{pmatrix} = \mathbf{R} \begin{pmatrix} \frac{\partial \varepsilon_{nn}}{\partial \xi} & \frac{\partial \varepsilon_{nt}}{\partial \xi} \\ \frac{\partial \varepsilon_{nt}}{\partial \xi} & \frac{\partial \varepsilon_{tt}}{\partial \xi} \end{pmatrix} \mathbf{R}^\top, \quad \begin{pmatrix} \frac{\partial \phi_x}{\partial \xi} \\ \frac{\partial \phi_y}{\partial \xi} \end{pmatrix} = \mathbf{R} \begin{pmatrix} \frac{\partial \phi_n}{\partial \xi} \\ \frac{\partial \phi_t}{\partial \xi} \end{pmatrix},$$

or in explicit form

$$(87) \quad \frac{\partial \chi}{\partial \xi} = \begin{pmatrix} \frac{\partial \varepsilon_{xx}}{\partial \xi} \\ \frac{\partial \varepsilon_{xy}}{\partial \xi} \\ \frac{\partial \varepsilon_{yy}}{\partial \xi} \\ \frac{\partial \phi_x}{\partial \xi} \\ \frac{\partial \phi_y}{\partial \xi} \end{pmatrix} = \begin{pmatrix} \frac{\partial \varepsilon_{nn}}{\partial \xi} n_x^2 + 2 \frac{\partial \varepsilon_{nt}}{\partial \xi} n_x t_x + \frac{\partial \varepsilon_{tt}}{\partial \xi} t_x^2 \\ \frac{\partial \varepsilon_{nn}}{\partial \xi} n_x n_y + \frac{\partial \varepsilon_{nt}}{\partial \xi} (t_y n_x + t_x n_y) + \frac{\partial \varepsilon_{tt}}{\partial \xi} t_x t_y \\ \frac{\partial \varepsilon_{nn}}{\partial \xi} n_y^2 + \frac{\partial \varepsilon_{nt}}{\partial \xi} n_y t_y + \frac{\partial \varepsilon_{tt}}{\partial \xi} t_y^2 \\ \frac{\partial \phi_n}{\partial \xi} n_x + \frac{\partial \phi_t}{\partial \xi} t_x \\ \frac{\partial \phi_n}{\partial \xi} n_y + \frac{\partial \phi_t}{\partial \xi} t_y \end{pmatrix}.$$

To impose the viscous conditions, we modify (87) by eliminating the appropriate normal-normal, normal-tangential and tangential-tangential derivative of the rate-of-strain tensor and/or the normal derivative of the temperature gradient, which for a constant viscosity  $\mu$  and constant heat conductivity  $\kappa$  is equivalent to imposing the deviatoric stress tensor gradient  $\boldsymbol{\tau}$  and heat flux gradient  $\mathbf{q}$ , respectively. For example, imposing

$$\frac{\partial(\mathbf{t}^\top \boldsymbol{\tau} \mathbf{n})}{\partial \xi} = 0, \quad \frac{\partial(\mathbf{q} \cdot \mathbf{n})}{\partial \xi} = 0,$$

on a subsonic outflow (see Subsection 2.2.1), yields the following modified normal derivative

$$(88) \quad \frac{\partial \tilde{\chi}}{\partial \xi} = \begin{pmatrix} \frac{\partial \varepsilon_{nn}}{\partial \xi} n_x^2 + \frac{\partial \varepsilon_{tt}}{\partial \xi} t_x^2 \\ \frac{\partial \varepsilon_{nn}}{\partial \xi} n_x n_y + \frac{\partial \varepsilon_{tt}}{\partial \xi} t_x t_y \\ \frac{\partial \varepsilon_{nn}}{\partial \xi} n_y^2 + \frac{\partial \varepsilon_{tt}}{\partial \xi} t_y^2 \\ \frac{\partial \phi_t}{\partial \xi} t_x \\ \frac{\partial \phi_t}{\partial \xi} t_y \end{pmatrix}.$$

Ultimately, we replace  $\mathbf{V}$  in (81) by the modified viscous contributions

$$(89) \quad \tilde{\mathbf{v}} = \frac{1}{\text{Re}_\infty} \left[ \mathbf{A}_n^{U_h} \frac{\partial \mathbf{U}_h}{\partial \xi} + \mathbf{A}_n^{\chi_h} \frac{\partial \tilde{\chi}_h}{\partial \xi} + \mathbf{A}_t^{U_h} \frac{\partial \mathbf{U}_h}{\partial \eta} + \mathbf{A}_t^{\chi_h} \frac{\partial \chi_h}{\partial \eta} \right],$$

where all derivatives are evaluated at the interior state  $\mathbf{U}_h$  and  $\chi_h$ .

To conclude this section, we provide a summary of all introduced target states and boundary conditions in Table 1 and Table 2, respectively. Recall that the difference between the Navier-Stokes characteristic boundary conditions (NSCBCs) of Subsection 4.1 and the generalized relaxation boundary conditions (GRCBCs) of Subsection 4.2 solely lies in the definition of the relaxation matrix  $\widehat{\mathbf{D}}$ . Furthermore, the definition of the characteristic boundary operator (CBC) in Table 2 has been derived assuming an implicit Euler time marching scheme, see Remark 4.1. Adapting the characteristic boundary operator (CBC) to a different time discretization scheme is straightforward and can be accomplished by following the same procedure outlined in this section.

	Target state	$\mathbf{U}^-$
$\mathbf{U}_{p_\infty}$	Pressure state	$(\rho_h, \rho \mathbf{u}_h, p_\infty/(\gamma - 1) + \rho_h  \mathbf{u}_h ^2/2)^\top$
$\mathbf{U}_\infty$	Far-field state	$(\rho_\infty, \rho_\infty \mathbf{u}_\infty, \rho_\infty E_\infty)^\top$
$\mathbf{U}_{\rho \mathbf{u}_\infty}$	Mass state	$(\rho_\infty, \rho \mathbf{u}_\infty, p_h/(\gamma - 1) + \rho_\infty  \mathbf{u}_\infty ^2/2)^\top$
$\mathbf{U}_{\theta_\infty}$	Entropy State	$\rho_\infty (\theta_h/\theta_\infty)^{1/(\gamma-1)} (1, \mathbf{u}_\infty, \theta_h/\gamma +  \mathbf{u}_\infty ^2/2)^\top$

TABLE 1. Summary of target states

	Boundary type	$\widehat{\Gamma}_h$
$\widehat{\Gamma}_{ad}$	Adiabatic wall	$(\widehat{\rho}_h - \rho_h, \widehat{\rho} \mathbf{u}_h, 1/(\text{Re}_\infty \text{Pr}_\infty) \phi_h \cdot \mathbf{n})^\top - \mathbf{S}_d (0, \mathbf{0}, \rho E_h - \widehat{\rho} E_h)^\top$
$\widehat{\Gamma}_{iso}$	Isothermal wall	$\widehat{\mathbf{U}}_h - (\rho_h, \mathbf{0}, \rho_h \theta_{\text{wall}}/\gamma)^\top$
$\widehat{\Gamma}_{inv}$	Inviscid wall	$\widehat{\mathbf{U}}_h - (\rho_h, (\mathbf{I} - \mathbf{n} \otimes \mathbf{n}) \rho \mathbf{u}_h, \rho E_h)^\top$
$\widehat{\Gamma}_{p_\infty}$	Subsonic outflow	$\widehat{\mathbf{U}}_h - \mathbf{U}_{p_\infty}$
$\widehat{\Gamma}_\infty$	Far-field	$\widehat{\mathbf{A}}^+(\widehat{\mathbf{U}}_h - \mathbf{U}_h) - \widehat{\mathbf{A}}^-(\widehat{\mathbf{U}}_h - \mathbf{U}_\infty)$
$\widehat{\Gamma}_C$		$\widehat{\mathbf{A}}^+(\widehat{\mathbf{U}}_h - \mathbf{U}_h) - \widehat{\mathbf{A}}^-(\widehat{\mathbf{U}}_h - \widehat{\mathbf{U}}_h^n + \Delta t [\widehat{\mathbf{P}} \widehat{\mathbf{D}} \widehat{\mathbf{P}}^{-1} (\widehat{\mathbf{U}}_h - \mathbf{U}^-)])$
$\widehat{\Gamma}_C^{\mathcal{T}}$	CBC	$\widehat{\mathbf{A}}^+(\widehat{\mathbf{U}}_h - \mathbf{U}_h) - \widehat{\mathbf{A}}^-(\widehat{\mathbf{U}}_h - \widehat{\mathbf{U}}_h^n + \Delta t [\widehat{\mathbf{P}} \widehat{\mathbf{D}} \widehat{\mathbf{P}}^{-1} (\widehat{\mathbf{U}}_h - \mathbf{U}^-) + \beta \widehat{\mathbf{B}} \frac{\partial \widehat{\mathbf{U}}}{\partial \eta}])$
$\widehat{\Gamma}_C^{\mathcal{T}\mathbf{v}}$		$\widehat{\mathbf{A}}^+(\widehat{\mathbf{U}}_h - \mathbf{U}_h) - \widehat{\mathbf{A}}^-(\widehat{\mathbf{U}}_h - \widehat{\mathbf{U}}_h^n + \Delta t [\widehat{\mathbf{P}} \widehat{\mathbf{D}} \widehat{\mathbf{P}}^{-1} (\widehat{\mathbf{U}}_h - \mathbf{U}^-) + \beta \widehat{\mathbf{B}} \frac{\partial \widehat{\mathbf{U}}}{\partial \eta} - \tilde{\mathbf{v}}])$

TABLE 2. Summary of boundary conditions

## 5. NUMERICAL EXPERIMENTS

The implementation of the characteristic boundary conditions described in Section 4 has been evaluated by four benchmarks in a two-dimensional setting, inspired by [12, 24]. Every numerical experiment includes a comparison of the numerical solution against the exact solution, if available; otherwise, it is compared against a reference solution. The latter is computed in a larger reference domain  $\Omega_r$  equipped with appropriate non-reflecting closures at the boundaries and, if deemed necessary, with sponge layers to dampen incoming disturbances. One of the

metrics we use are the scaled  $L_2(\Omega)$ -errors of the discrete pressure  $p_h$ , with respect to the reference/exact solution  $p_r$ , that is

$$e_p := \frac{\|p_h - p_r\|}{\|p_r\|}.$$

Additionally, the results are compared to common boundary conditions in the HDG framework, namely the subsonic outflow (SO) boundary condition (52) and the far-field (FF) boundary condition (54). To distinguish between the Navier-Stokes characteristic boundary conditions (NSCBCs) of Subsection 4.1 and the generalized characteristic relaxation boundary conditions (GRCBCs) of Subsection 4.2, the different relaxation matrices  $\widehat{\mathbf{D}}$ , the different target states  $\mathbf{U}^-$ , the inclusion of tangential convection contributions  $\mathcal{T}^-$  and the viscous terms  $\mathcal{V}$  we introduce the following notation:

- The type of characteristic boundary condition is denoted by the abbreviation NSCBC or GRCBC.
- The value of the user-required inputs of the relaxation matrices  $\widehat{\mathbf{D}}$ , is displayed as subscript, e.g., GRCBC<sub>0.01</sub>. For the sake of simplicity, we assumed a single user-value for all components of the relaxation matrix i.e. for the GRCBCs we solely imposed  $C_i = C$ , see (73), while for the NSCBCs we set  $\sigma_i = \sigma$  and  $L = 1$ , see (37) and (45).
- For subsonic outflows we introduced the target states  $\mathbf{U}_{p_\infty}$  and  $\mathbf{U}_\infty$ , while for subsonic inflows we introduced  $\mathbf{U}_\infty$ ,  $\mathbf{U}_{\rho u_\infty}$  and  $\mathbf{U}_{\theta_\infty}$ . The type of target state,  $\mathbf{U}^-$ , is denoted by the corresponding subscript, e.g., GRCBC<sub>0.01 $p_\infty$</sub>  for the target state  $\mathbf{U}_{p_\infty}$ .
- If tangential convective contributions  $\mathcal{T}$  are included, the symbol  $\mathcal{T}$  is denoted in the superscript, e.g., GRCBC $\mathcal{T}$ <sub>0.01 $p_\infty$</sub> . The tangential relaxation parameter  $\beta$  is set to  $\text{Ma}_\infty$  in all cases.
- If viscous contributions  $\mathcal{V}$  are included, the symbol  $\mathcal{V}$  is denoted in the superscript, e.g., GRCBC $\mathcal{T}\mathcal{V}$ <sub>0.01 $p_\infty$</sub> .

A calorically perfect gas with specific heat ratio  $\gamma = 1.4$ , Prandtl number  $\text{Pr}_\infty = 0.72$  and with constant viscosity  $\mu = 1$  is considered. Unless specified otherwise, the spatial discretization employs a polynomial order  $k = 4$ , time-stepping is performed using an implicit BDF2 scheme with a suitable time step  $\Delta t$ , and the convective and viscous stabilization matrices are defined as  $\mathbf{S}_c = \widehat{\mathbf{A}}^+$  and  $\mathbf{S}_d = \text{diag}(0, \mathbf{1}, 1/\text{Pr}_\infty)/\text{Re}_\infty$ , respectively.

The numerical experiments have been conducted using the open-source python extension `DreAm`, which is built on the open-source finite element library `NGSolve` [37]. Simulation data is publicly available in the `Zenodo` repository [38].

**5.1. Planar acoustic pulse.** The first benchmark consists of an inviscid one-dimensional downstream  $\mathbf{u}^+$ /upstream  $\mathbf{u}^-$  propagating linear acoustic pulse, similar to [24], in a domain  $\Omega = (-4X, 4X) \times (-0.14, 0.14)$  depicted in Figure 4. In order to mimic a one-dimensional domain, the upper and lower boundaries  $\Gamma_{\text{periodic}}$  are coupled periodically.

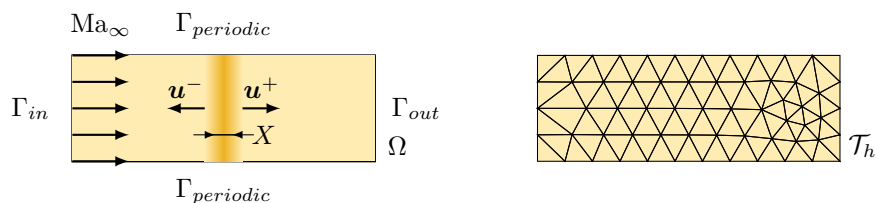


FIGURE 4. Representation of the domain  $\Omega$  with corresponding boundaries  $\Gamma$  and the triangulation  $\mathcal{T}_h$  with mesh size  $h = 0.035$ .

The acoustic pulse is initialized at  $t = 0$  with the initial conditions given as

$$\rho_0 = \rho_\infty, \quad \mathbf{u}_0^\pm = \mathbf{u}_\infty \left( 1 \pm \frac{p_\infty}{\rho_\infty c_\infty} \frac{\alpha}{|\mathbf{u}_\infty|} \exp\left(-x^2/X^2\right) \right), \quad p_0 = p_\infty \left( 1 + \alpha \exp\left(-x^2/X^2\right) \right),$$

where  $X = 0.1$  denotes the extent of the acoustic pulse and  $\alpha$  the pulse strength. The constant uniform flow  $\mathbf{u}_\infty$  ensures the correct physical behavior at the subsonic inflow boundary  $\Gamma_{in}$  and subsonic outflow boundary  $\Gamma_{out}$ . Note that we use acoustic scaling, see (2b), with dimensionless quantities  $\rho_\infty = 1$ ,  $|\mathbf{u}_\infty| = \text{Ma}_\infty = 0.03$ ,  $c_\infty = 1$  and  $p_\infty = 1/\gamma$ .

Every simulation is performed up to a dimensionless time  $t_{end} = 5$  with time step  $\Delta t = 2 \cdot 10^{-3}$ . As a reference solution we use a computed solution in a larger domain  $\Omega_r = (-14X, 14X) \times (-0.14, 0.14)$  in which the acoustic pressure pulse propagates undisturbed through the domain during the time interval  $(0, t_{end}]$  without impinging on the boundaries. In addition to the scaled  $L_2(\Omega)$ -errors of the pressure  $e_p$ , we rely on the mean incoming acoustic  $\bar{w}^-$  and outgoing  $\bar{w}^+$  acoustic characteristics at the boundaries  $\Gamma_{in}$  and  $\Gamma_{out}$  to assess the quality of the numerical solution. These are defined as

$$w^\mp := (p_h - p_\infty) \mp \rho_h c_h (\mathbf{u}_h - \mathbf{u}_\infty) \cdot \mathbf{n}, \quad \bar{w}^\mp := \frac{1}{|\Gamma|} \int_\Gamma w^\mp ds,$$

respectively. Further, for the upstream propagating pulse, we consider the mean entropy wave

$$w^s := c_h^2 (\rho_h - \rho_\infty) - (p_h - p_\infty), \quad \bar{w}^s := \frac{1}{|\Gamma_{in}|} \int_{\Gamma_{in}} w^s ds,$$

at the boundary  $\Gamma_{in}$ , since this characteristic wave is determined from upstream in the case of subsonic inflow.

In order to investigate the effect of the relaxation matrix  $\widehat{\mathbf{D}}$  on the reflection of the acoustic pulse, we consider three different relaxation coefficients  $C = [0.1, 0.01, 0.0]$  for the GRCBCs and  $\sigma = [1.0, \sigma_{opt}, 0.0]$  for the NSCBCs, where  $\sigma_{opt} = 0.28$  is approximately the optimal relaxation parameter for a subsonic outflow, as described in Subsection 2.2.1.

For a linear acoustic pulse with strength  $\alpha = 0.001$ , the mean incoming  $\bar{w}^-$  and outgoing  $\bar{w}^+$  acoustic characteristics for the downstream propagating pulse are shown in Figure 5, while the

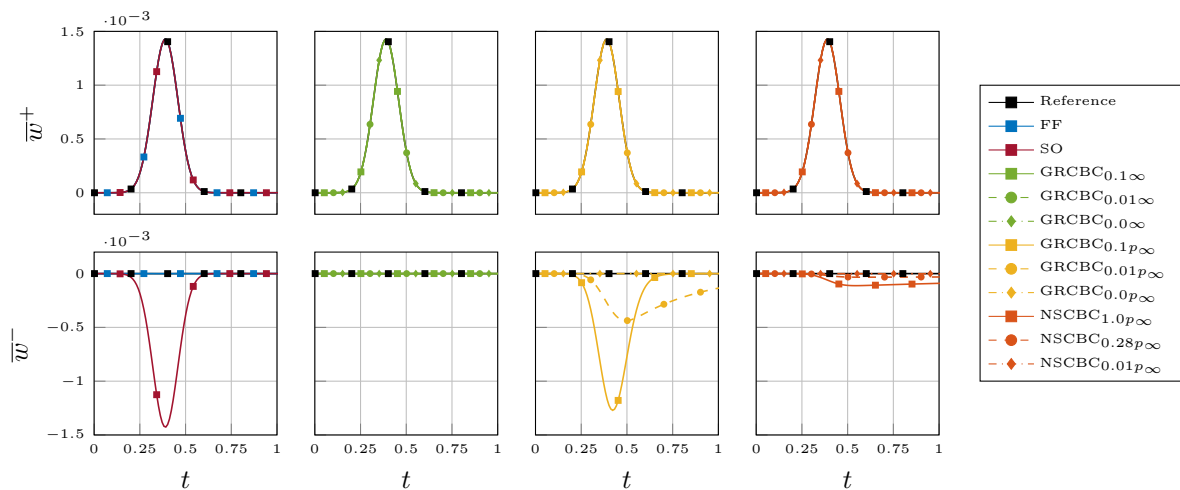


FIGURE 5. Downstream propagating linear acoustic pulse with strength  $\alpha = 0.001$ : incoming  $\bar{w}^-$  and outgoing  $\bar{w}^+$  acoustic characteristics at the boundary  $\Gamma_{out}$ .

upstream propagation pulse are shown in Figure 6. The scaled errors  $e_p$  for the downstream and upstream propagating pulse are shown in Figure 7 and Figure 8, respectively.

From the figures it is evident that the far-field boundary condition (—■— FF) and the characteristic boundary conditions with target state  $\mathbf{U}_\infty$  (—■— GRCBC $_\infty$ ) closely match the reference solution for both the downstream and upstream propagating acoustic pulse. In contrast, simulations enforcing the static pressure  $\mathbf{U}_{p_\infty}$  at the outflow  $\Gamma_{out}$  (—■— SO, —■— GRCBC $_{p_\infty}$ , —■— NSCBC $_{p_\infty}$ ) and either the mass flux  $\mathbf{U}_{\rho u}$  or the static temperature  $\mathbf{U}_{\theta_\infty}$  at the inflow  $\Gamma_{in}$  (—■— GRCBC $_{\rho u_\infty}$ , —■— GRCBC $_{\theta_\infty}$ ), result in total/partial reflection of the acoustic pulse. This behavior is expected, as the imposition of hard boundaries inevitably leads to a reflection of the

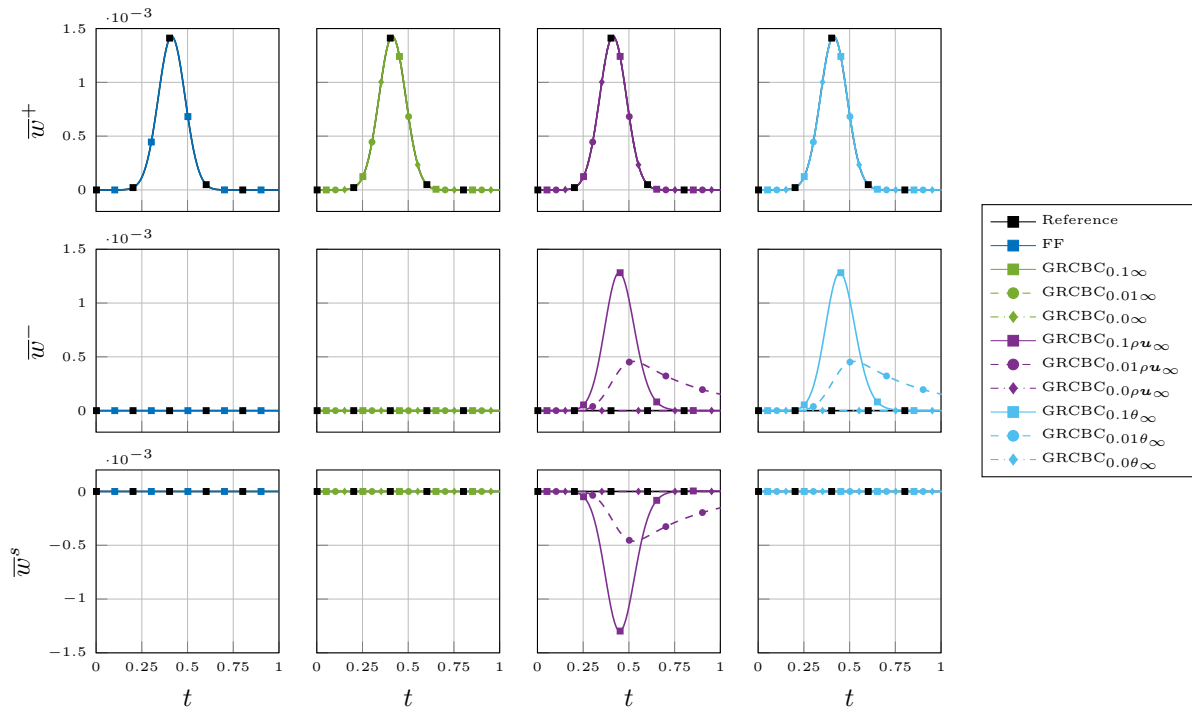


FIGURE 6. Upstream propagating linear acoustic pulse with strength  $\alpha = 0.001$ : incoming  $\bar{w}^-$  and outgoing  $\bar{w}^+$  acoustic characteristics and incoming entropy wave  $\bar{w}^s$  at the boundary  $\Gamma_{in}$ .

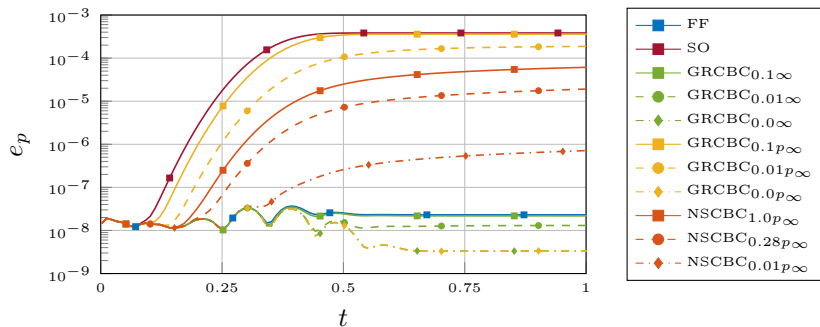


FIGURE 7. Downstream propagating linear acoustic pulse with strength  $\alpha = 0.001$ : scaled  $L_2(\Omega)$ -errors of the pressure  $e_p$ .

acoustic pulse. Interestingly, the reflection at the inflow  $\Gamma_{in}$  for the mass flux target state  $U_{\rho u}$  leads to an incoming entropy wave  $\bar{w}^s$ , which is absent when imposing the static temperature  $U_{\theta_\infty}$ , due to the underlying isentropic relation (71).

A way to overcome the reflective issue within the context of a one-dimensional perturbation is by tuning the amount of relaxation  $\widehat{D}$  towards the target state  $U^-$ , as discussed in Subsection 2.2.1. For every characteristic boundary condition (GRCBC, NSCBC) under evaluation, we observe a significant reduction in the reflection for vanishing relaxation matrix  $\widehat{D} \rightarrow \mathbf{0}$ , to the point of perfect non-reflecting behavior. Nevertheless, the results of the linear acoustic pulse suggest that for a purely planar acoustic perturbation, the far-field target state,  $U_\infty$ , appears to be the most appropriate choice, without requiring precise tuning of the relaxation matrix  $\widehat{D}$ .

**5.2. Oblique pressure pulse.** This benchmark involves analyzing the propagation of a cylindrical non-linear pressure pulse within a squared domain  $\Omega = (-5R, 5R) \times (-5R, 5R)$  as shown in Figure 9, where  $R = 0.2$  is the radius of the initial perturbation. The objective is to examine the non-reflective performance of the newly implemented characteristic boundary conditions

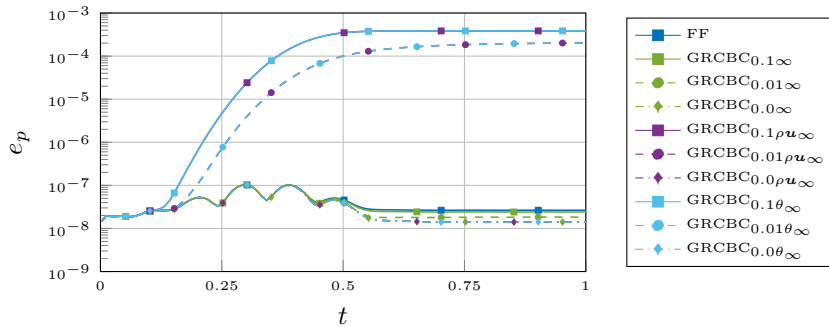


FIGURE 8. Upstream propagating linear acoustic pulse with strength  $\alpha = 0.001$ : scaled  $L_2(\Omega)$ -errors of the pressure  $e_p$ .

when oblique waves impinge on the boundaries, as well as the alternating inflow and outflow behavior at the boundaries triggered by the pressure pulse. The initial conditions are given as

$$\rho_0 = \rho_\infty, \quad \mathbf{u}_0 = \mathbf{0}, \quad p_0 = p_\infty \left( 1 + \alpha \exp\left(-r^2/R^2\right) \right),$$

where  $\alpha = 0.5$  is the pulse strength and  $r^2 = x^2 + y^2$  the polar coordinate [24]. Initially, the fluid is at rest, which translates to  $\text{Ma}_\infty = 0$ , necessitating the adoption of acoustic scaling (2b) of the Euler equations with dimensionless quantities  $\rho_\infty = 1$ ,  $c_\infty = 1$  and  $p_\infty = 1/\gamma$ , since for an aerodynamic scaling the speed of sounds tends to  $c_\infty \rightarrow \infty$ . Further, due to the absence of a baseflow, the convective stabilization matrix is chosen as a Lax-Friedrichs [34]  $\mathbf{S}_c = \max(|\hat{u}_n| + \hat{c}, 0)\mathbf{I}$ .

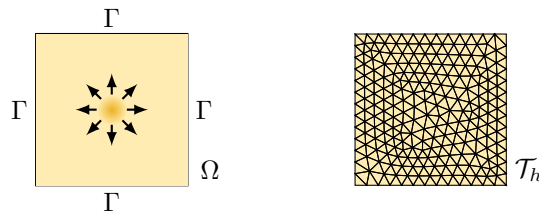


FIGURE 9. Representation of the domain  $\Omega$  with corresponding boundaries  $\Gamma$  and triangulation  $\mathcal{T}_h$  with mesh size  $h = 0.15$ .

Similarly to the one-dimensional acoustic pulse, we compute a reference solution in a larger circular domain  $\Omega_r = \{(x, y) : x^2 + y^2 \leq 40R\}$ , where the pressure pulse propagates undisturbed through the domain during the time interval  $(0, t_{end}]$  without impinging on the boundaries. The time-stepping is performed with a time step  $\Delta t = 2 \cdot 10^{-3}$  up to a dimensionless time  $t_{end} = 4$ . Besides the scaled  $L_2(\Omega)$ -errors of the pressure  $e_p$ , in Figure 10 we show the  $L_2(\Omega)$ -norm of the scaled fluctuating pressure

$$(90) \quad \Delta \tilde{p} := \frac{p_h - p_\infty}{p_\infty},$$

to visualize the propagation of the reference solution. Note that we excluded the simulation results with no relaxation ( $\widehat{\mathbf{D}} = \mathbf{0}$ ), since they almost coincide with the far-field solution (—■— FF), in accordance to the observations drawn from Subsection 5.1. Similarly, also the cases with a large relaxation and target state  $\mathbf{U}_{p_\infty}$  are omitted, as they produce the same outcome as the subsonic outflow boundary condition (—■— SO). In Figure 11, the snapshots of the scaled fluctuating pressure  $\Delta \tilde{p}$  are reported at time instances  $t_0 = 0.75$ ,  $t_1 = 1$  and  $t_2 = 1.25$ , during which the pressure pulse intersects the boundaries.

In Figure 10b we observe that at  $t = t_{end}$  the reference solution (—■— Reference) has not yet recovered the target pressure  $p_\infty$ , indicating that the decay of the initial non-linear pressure pulse is progressing slowly. Analogous to the findings from the one-dimensional acoustic pulse, any

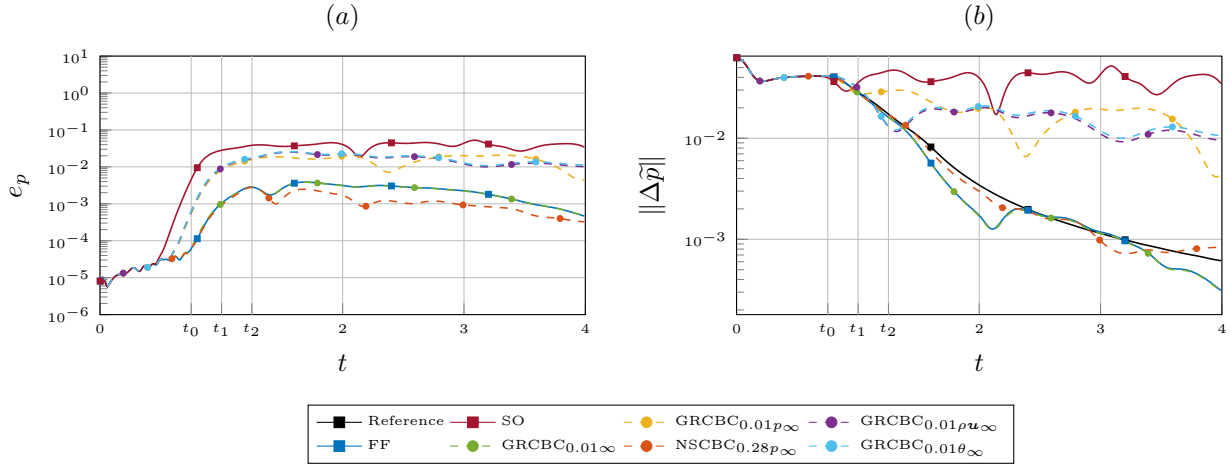


FIGURE 10. Pressure pulse with strength  $\alpha = 0.5$ : (a) scaled  $L_2(\Omega)$ -errors of the pressure  $e_p$  and (b)  $L_2(\Omega)$ -norm of the scaled fluctuating pressure  $\Delta\tilde{p}$ .

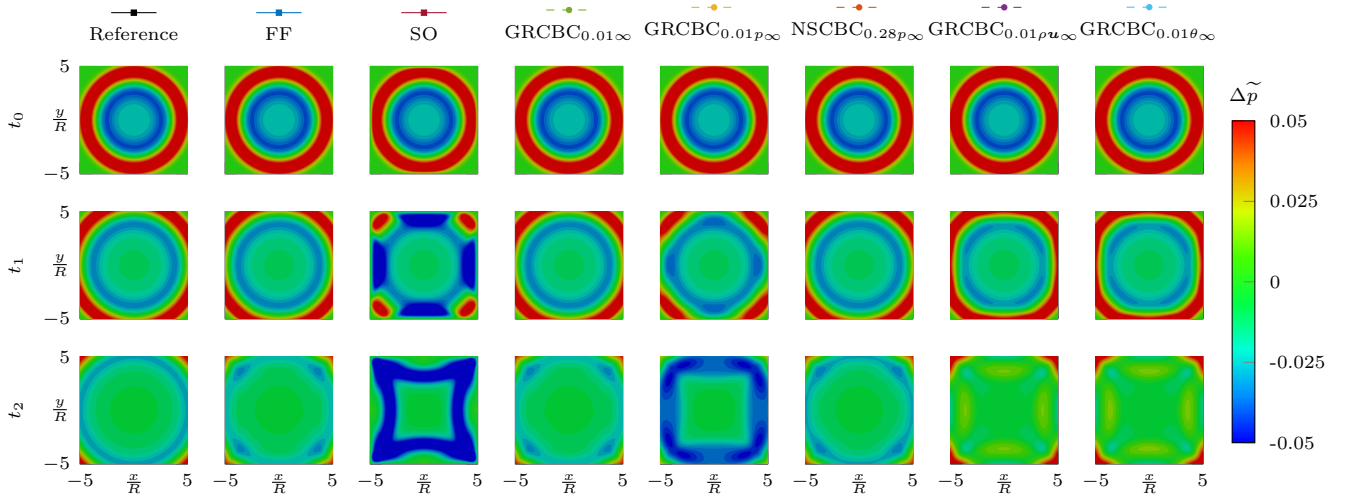


FIGURE 11. Pressure pulse with strength  $\alpha = 0.5$ : scaled fluctuating pressure  $\Delta\tilde{p}$  for different boundary conditions at time instances  $t_0 = 0.75$ ,  $t_1 = 1$  and  $t_2 = 1.25$ .

imposition of a hard boundary condition leads to a full/partial reflection of the pressure pulse depending on the relaxation amount in the relaxation matrix  $\widehat{\mathbf{D}}$ , as can be seen in Figure 10 and in Figure 11. The subsonic outflow boundary condition ( $\blacksquare$  SO) and the characteristic boundary conditions ( $\bullet$  GRCBC $_{p_\infty}$ ,  $\bullet$  GRCBC $_{\rho u_\infty}$ ,  $\bullet$  GRCBC $_{\theta_\infty}$ ) generate the most amount of perturbations, although the latter can be tuned appropriately to reduce the reflections by adjusting the relaxation matrix  $\widehat{\mathbf{D}}$ . Remarkably, the boundary condition ( $\bullet$  NSCBC $_{0.28p_\infty}$ ) with the pressure target state  $\mathbf{U}_{p_\infty}$  and the optimal determined relaxation parameter  $\sigma_{opt} = 0.28$ , see Subsection 2.2.1, shows the smallest reflection of the pressure pulse. Boundary conditions using the far-field state  $\mathbf{U}_\infty$  ( $\blacksquare$  FF,  $\bullet$  GRCBC $_\infty$ ) seem to be an appropriate choice for a pressure pulse, as they exhibit little reflection and are not sensitive to the alternating change of inflow and outflow, even though in the interval  $t_1 < t < 2$  they dampen the numerical solution slightly more than the reference solution. This overdamping is likely caused by the absence of transverse terms in the boundary conditions, which are crucial for the accurate propagation of the pressure pulse within the domain. This effect is evident in the discrepancy between the

reference solution and the simulation results at the corners of the domain (see snapshot  $t_2$  in Figure 11).

**5.3. Zero-circulation vortex.** The aim of this benchmark is to investigate the non-reflecting behavior of newly implemented boundary conditions in presence of vortical structures in a low-Mach flow. Particularly, we expect a significant improvement in the accuracy of the solution on outflow boundaries, in combination with the transverse relaxation parameter  $\beta$ , emerging from a low-Mach asymptotic analysis as described in Section 2.

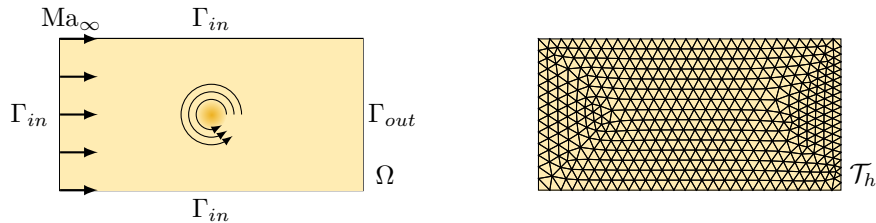


FIGURE 12. Representation of the domain  $\Omega$  with corresponding boundaries  $\Gamma$  and the triangulation  $\mathcal{T}_h$  with mesh size  $h = 0.15$  and local mesh size  $h_{out} = 0.1$  at  $\Gamma_{out}$ .

A cylindrical, zero-circulation vortex of radius  $R = 0.1$  is injected into an inviscid baseflow with Mach number  $\text{Ma}_\infty$ . The domain consists of a rectangle  $\Omega = (-20R, 20R) \times (-10R, 10R)$  and in the initial configuration  $t = 0$  the vortex is located at the origin  $\mathbf{x}_0 = (0, 0)$ , as shown in Figure 12. The initial conditions are

$$\begin{aligned} \rho_0 &= \rho_\infty \left( 1 - \frac{\gamma - 1}{2} \text{Ma}_\infty^2 \alpha^2 \exp\left(1 - r^2/R^2\right) \right)^{1/(\gamma-1)}, \\ \mathbf{u}_0 &= |\mathbf{u}_\infty| \left[ \begin{pmatrix} 1 \\ 0 \end{pmatrix} + \begin{pmatrix} -y \\ x \end{pmatrix} \frac{\alpha}{R} \exp\left(\frac{1}{2} \left(1 - r^2/R^2\right)\right) \right], \\ p_0 &= p_\infty \left( 1 - \frac{\gamma - 1}{2} \text{Ma}_\infty^2 \alpha^2 \exp\left(1 - r^2/R^2\right) \right)^{\gamma/(\gamma-1)}, \end{aligned}$$

where the polar coordinate  $r$  is given as  $r^2 = (x - x_0)^2 + (y - y_0)^2$  and  $\alpha$  denotes the vortex strength ratio of the vortex to the base flow,  $\text{Ma}_v = \alpha \text{Ma}_\infty$ , studied in the following subsections. We employ aerodynamic scaling, see (2a), with dimensionless quantities  $\rho_\infty = 1$ ,  $|\mathbf{u}_\infty| = 1$  and  $p_\infty = 1/(\text{Ma}_\infty^2 \gamma)$ . The time-stepping is performed with a time step  $\Delta t = 2 \cdot 10^{-3}$  up to a dimensionless time  $t_{end} = 5$ .

We expect that most reflections will be generated while the vortex intersects the outflow boundary  $\Gamma_{out}$ . Dimensional analysis indicates that this intersection occurs at approximately  $t \approx 2$ . Consequently, the primary objective of this benchmark is to evaluate the non-reflecting behavior of the subsonic outflow boundary conditions.

At the subsonic inflows  $\Gamma_{in}$  we expect upstream traveling acoustic waves. Given the good results of the far-field target state  $\mathbf{U}_\infty$  for acoustic perturbations in previous benchmarks, we impose a  $\text{GRCBC}_{0.01\infty}$  as the closure condition.

Since the transverse relaxation parameter  $\beta$  is derived from a low-Mach asymptotic analysis, we consider an almost incompressible baseflow with a Mach number of  $\text{Ma}_\infty = 0.03$  and the commonly used limiting case for incompressible flow at  $\text{Ma}_\infty = 0.3$ .

An exact solution can be constructed by replacing  $\mathbf{x} = \mathbf{u}_\infty t + \mathbf{x}_0$ , since the vortex propagates at the speed and in the direction of the base flow  $\mathbf{u}_\infty$  due to the local equilibrium. In order to visualize the exact solution in our results, additionally to the scaled  $L_2(\Omega)$ -errors of the pressure  $e_p$ , we show the scaled fluctuating pressure  $\Delta \tilde{p}$  defined in (90).

Simulations conducted with increased relaxation parameters  $\widehat{D}$  confirm the observations from previous benchmarks, with higher relaxation increasingly reproducing the solutions of the common boundary conditions (—■— FF) and (—■— SO). Consequently, we only show results obtained with low relaxation parameters.

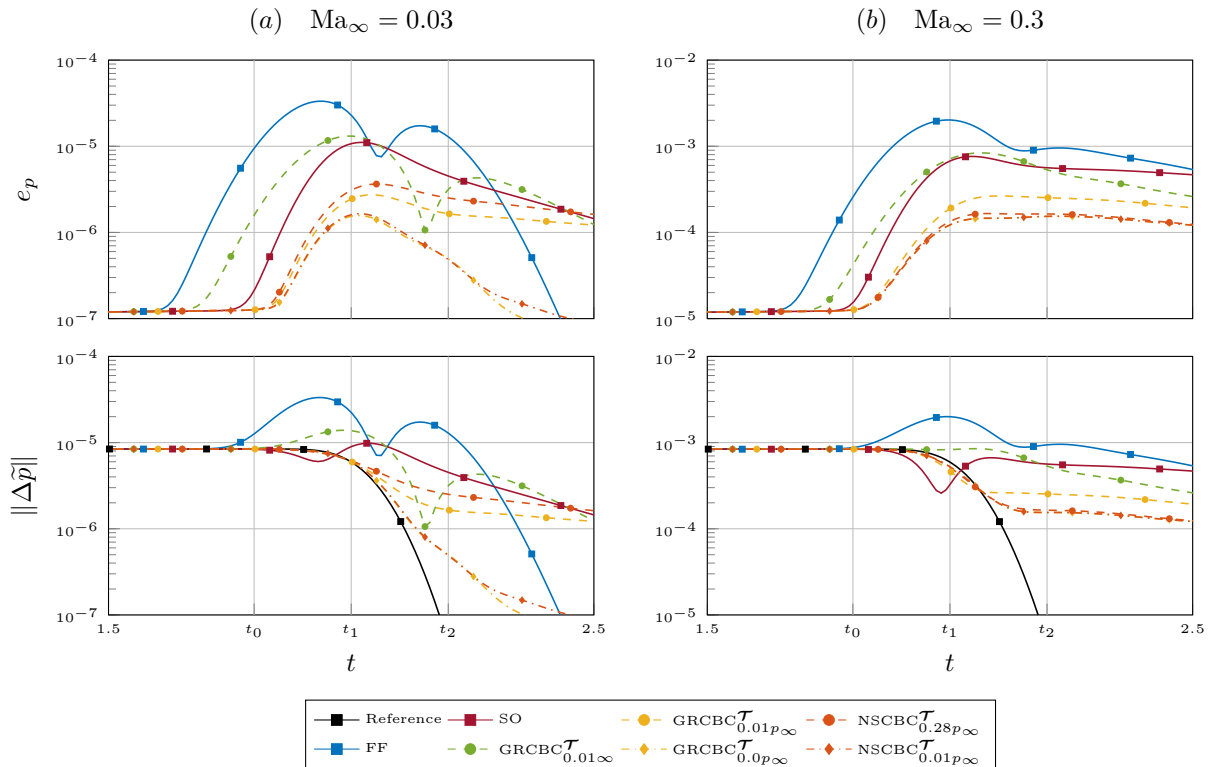


FIGURE 13. Zero-circulation vortex with vortex strength ratio  $\alpha = 1/3$ : scaled  $L_2(\Omega)$ -errors of pressure  $e_p$  and scaled pressure fluctuations  $\Delta\tilde{p}$  for Mach numbers (a)  $\text{Ma}_\infty = 0.03$  and (b)  $\text{Ma}_\infty = 0.3$ .

5.3.1. *Low vortex strength ratio  $\alpha = 1/3$ .* The first test consists of a vortex with a relatively low strength ratio  $\alpha = 1/3$ , in the sense that the subsonic outflow does not alternate to a subsonic inflow during the intersection of the vortex. Numerical results are shown in Figure 13, in which the scaled  $L_2(\Omega)$ -errors of the pressure  $e_p$  and the scaled pressure fluctuation  $\Delta\tilde{p}$  are shown for the two distinct baseflow Mach numbers  $\text{Ma}_\infty$ . In order to visually assess the performance of the boundary conditions, snapshots of the vorticity field and isocontour lines of the scaled fluctuating pressure  $\Delta\tilde{p}$  are shown for three time instances  $t_0 = 1.8$ ,  $t_1 = 2.0$  and  $t_2 = 2.2$  and Mach number  $\text{Ma}_\infty = 0.03$  in Figure 14.

As explained and observed in the earlier benchmarks, the subsonic outflow boundary condition ( $\blacksquare$  SO) causes considerable reflections at the outflow boundary  $\Gamma_{out}$ . Notably, the reflections are less intense than those generated by the far-field boundary condition ( $\blacksquare$  FF), which indicates that the subsonic outflow target state  $\mathbf{U}_{p_\infty}$  may be more appropriate in this scenario.

In comparison to the far-field boundary condition ( $\blacksquare$  FF), the CBCs with target state  $\mathbf{U}_\infty$  ( $\bullet$  GRCBC $\mathcal{T}_\infty$ ) show an improvement as they produce less reflections due to the inclusion of the transverse relaxation. Nevertheless, the imposition of the far-field target state  $\mathbf{U}_\infty$  on a subsonic outflow with exiting vortical structures is inappropriate and leads to a significant error in the solution, which is consistent with the findings of [12].

A notable improvement is achieved by the CBCs with target state  $\mathbf{U}_{p_\infty}$  ( $\bullet$  GRCBC $\mathcal{T}_{p_\infty}$ ,  $\bullet$  NSCBC $\mathcal{T}_{p_\infty}$ ) along with an additional transverse relaxation parameter  $\beta$ . In the plots of the scaled pressure fluctuation norm  $\|\Delta\tilde{p}\|$  in Figure 13, it is evident that these CBCs follow the exact solution closely during the crossover of the vortex, which is further supported by the snapshots of the vorticity field and the isocontour lines of the scaled fluctuating pressure  $\Delta\tilde{p}$  in Figure 14.

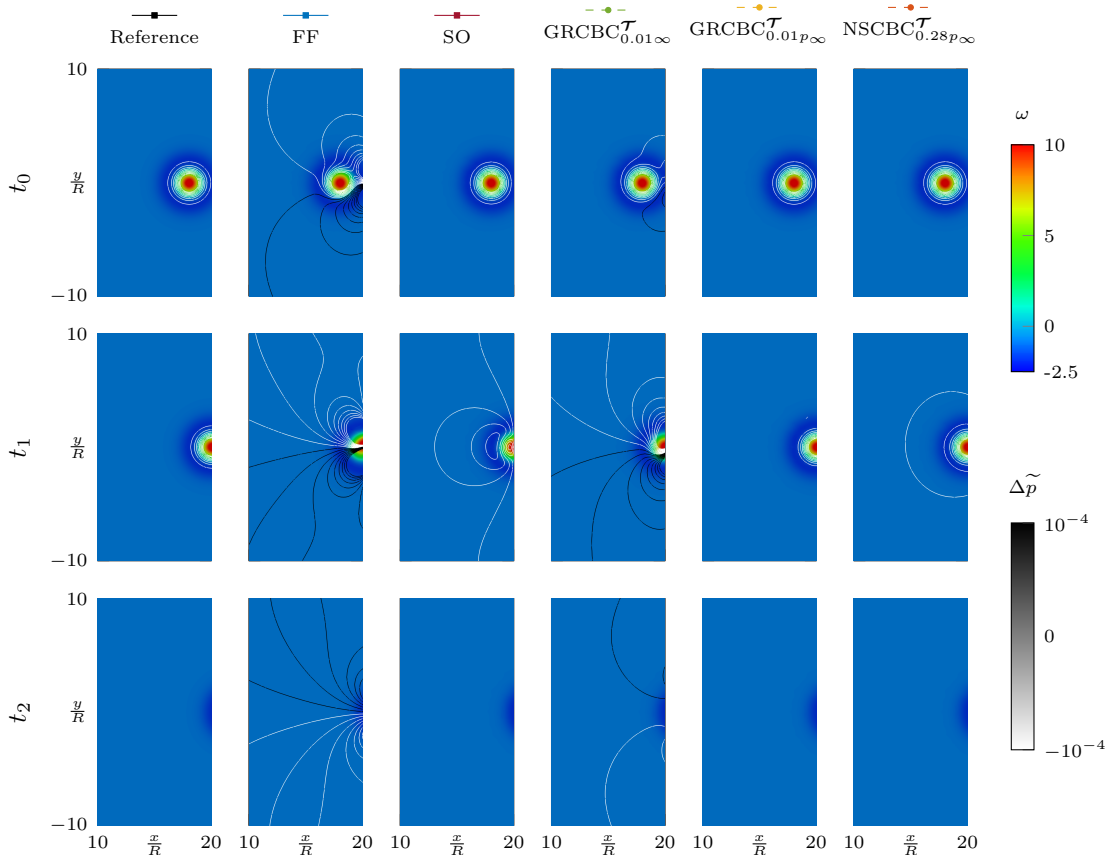


FIGURE 14. Zero-circulation vortex with vortex strength ratio  $\alpha = 1/3$  and Mach number  $\text{Ma}_\infty = 0.03$ : vorticity field  $\omega$  and isocontour lines of the scaled fluctuating pressure  $\Delta\tilde{p}$  for different boundary conditions at time instances  $t_0 = 1.8$ ,  $t_1 = 2.0$  and  $t_2 = 2.2$

These observations hold for both baseflow Mach numbers  $\text{Ma}_\infty$ , although for increasing Mach number the deviations from the exact solution become more pronounced, indicating the eventual limit of the low-Mach asymptotic analysis for the relaxation parameter  $\beta$ .

**5.3.2. High vortex strength ratio  $\alpha = 4/3$ .** The second vortex is characterized by a higher vortex strength ratio  $\alpha = 4/3$ , causing flow inversion to occur at the outflow boundary  $\Gamma_{out}$ . Results are displayed in Figure 15, where scaled  $L_2(\Omega)$ -errors of the pressure,  $e_p$ , and the scaled pressure fluctuation,  $\Delta\tilde{p}$ , are shown for the two distinct baseflow Mach numbers  $\text{Ma}_\infty$ .

Since the outflow target state  $\mathbf{U}_{p_\infty}$  is not an appropriate state to handle a subsonic inflow, the subsonic outflow condition ( $\blacksquare$  SO) is not well-defined anymore and diverges, due to the flow inversion at the outflow boundary. However, the CBCs ( $\bullet$  GRCBC $\mathcal{T}_{p_\infty}$ ,  $\bullet$  NSCBC $\mathcal{T}_{p_\infty}$ ), despite sharing the same target state  $\mathbf{U}_{p_\infty}$ , effectively manage the flow inversion, although producing relatively large reflections.

Boundary conditions ( $\blacksquare$  FF,  $\bullet$  GRCBC $\mathcal{T}_\infty$ ) with the far-field target state  $\mathbf{U}_\infty$  are by construction capable of handling flow inversion and seem to dampen the reflections more effectively than the CBCs with target state  $\mathbf{U}_{p_\infty}$ . Yet, the imposition of the far-field target state  $\mathbf{U}_\infty$  on a subsonic outflow boundary in the presence of vortices remains inappropriate.

For this vortex strength ratio, the effect of the transverse terms  $\mathcal{T}$  seems to be marginal. Although the relaxation parameter  $\beta$  causes a later deviation from the exact solution (see interval  $t_0 < t_1$ ) in comparison to ( $\blacksquare$  FF) and ( $\blacksquare$  SO), the incoming disturbances due to the flow inversion seem to be too strong to be effectively damped by the transverse relaxation.

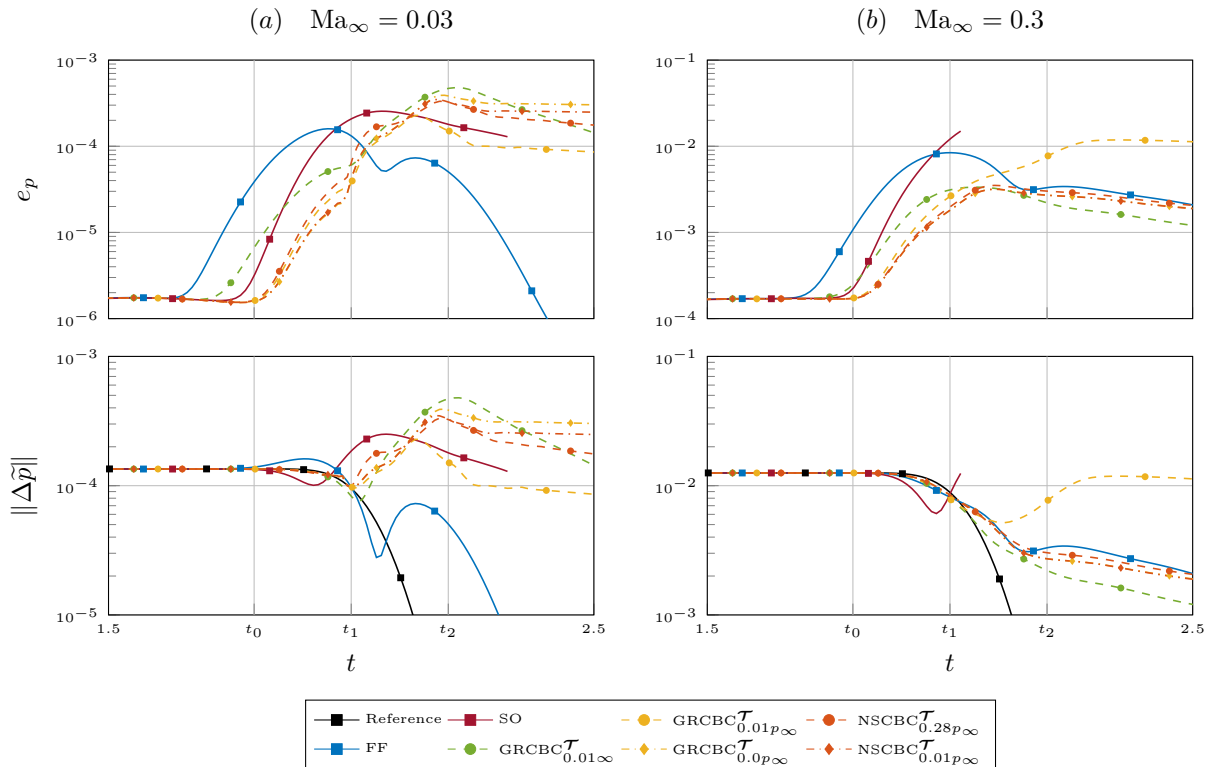


FIGURE 15. Zero-circulation vortex with vortex strength ratio  $\alpha = 4/3$ : scaled  $L_2(\Omega)$ -errors of pressure  $e_p$  and scaled pressure fluctuations  $\Delta\tilde{p}$  for Mach numbers (a)  $Ma_\infty = 0.03$  and (b)  $Ma_\infty = 0.3$ .

**5.4. Laminar flow around a cylinder.** The final benchmark involves a two-dimensional circular cylinder within a laminar viscous flow, incorporating all features from the previous benchmarks. Vortices, shed from the cylinder, generate alternating acoustic waves, resulting in a dipole sound, requiring the boundary conditions to be non-reflecting on the whole boundary. Additionally, the outflow boundary closure must be capable of handling the vortices crossing the artificial boundary without generating reflections.

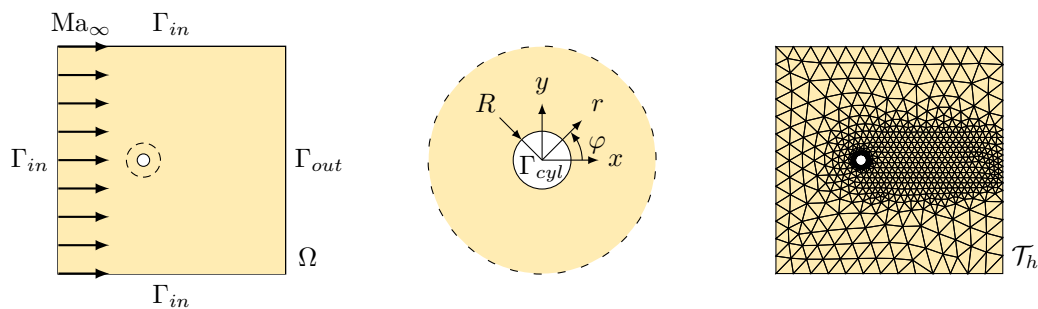


FIGURE 16. Representation of the domain  $\Omega$  with corresponding boundaries  $\Gamma$  and the triangulation  $\mathcal{T}_h$  with region dependent mesh size  $h$ .

Let  $\Omega = \{(x, y) \in (-15R, 25R) \times (-20R, 20R) \mid x^2 + y^2 \geq R^2\}$  be the computational domain with a circular cylinder of radius  $R = 0.5$ , as shown in Figure 16. The polar coordinates  $r, \varphi$  in counterclockwise direction are given as  $r^2 = x^2 + y^2$  and  $\tan \varphi = y/x$ .

An adiabatic wall boundary condition, as described in (51a), is enforced on the cylinder  $\Gamma_{cyl}$ . At the inflow boundaries  $\Gamma_{in}$ , we anticipate the presence of oblique impinging acoustic waves; therefore, we apply the characteristic boundary condition (GRCBC $_{0.01\infty}$ ), using the far-field

target state  $\mathbf{U}_\infty$  based on its strong performance in prior benchmarks. The subsonic outflow boundary  $\Gamma_{out}$ , where vortices shed from the cylinder interact with sound waves, poses the greatest challenge to manage, particularly due to its proximity to the cylinder. This boundary is the primary focus of the investigation of this test case.

We consider a Mach number of  $\text{Ma}_\infty = 0.2$  and a Reynolds number of  $\text{Re}_\infty = 150$ . In this setting the dimensionless vortex shedding frequency is known to be  $0.18 \leq St \leq 0.185$  [39], where  $St = fD/u_\infty$  is the Strouhal number,  $f$  the shedding frequency,  $D = 2R$  the cylinder diameter and  $u_\infty$  the free stream velocity. Every numerical investigation was initiated with a uniform flow at  $t = 0$  and advanced over time  $t = 250$  with time step  $\Delta t = 5 \cdot 10^{-2}$ , until the initial disturbances exited the domain. For an aerodynamic scaling (2a), the time step  $\Delta t$  corresponds to a Nyquist frequency of  $St_{ny} = 10$ , ensuring that the shedding frequency is well resolved. The simulation was then extended for a prolonged period,  $\bar{t} = \{t \mid 250 < t \leq 750\}$ , during which statistical data was collected over multiple shedding cycles.

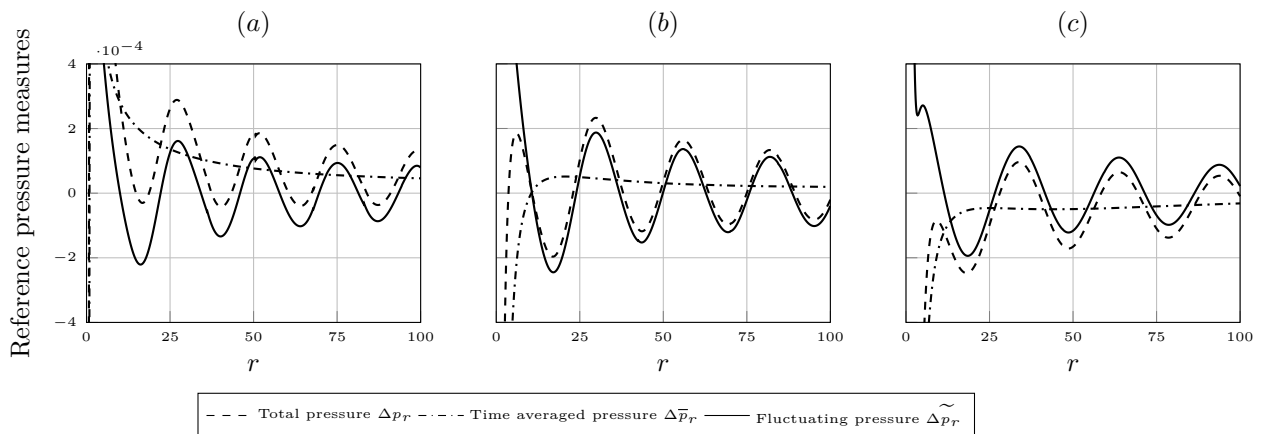


FIGURE 17. Laminar flow around a cylinder: plot of the reference solution pressure measures at angle (a)  $\varphi = 130^\circ$ , (b)  $\varphi = 101.5^\circ$  and (c)  $\varphi = 60^\circ$  over the radial coordinate  $r$  at time  $t = 731.55$ .

A reference solution has been generated in a reference domain  $\Omega_r = \{(x, y) \mid x^2 + y^2 \leq 1500^2\}$  by adding additional sponge layers to properly dampen all incoming disturbances. In Figure 17, the total pressure  $\Delta p$ , the time-averaged pressure  $\Delta \bar{p}$  over the time interval  $\bar{t}$  and the fluctuating pressure  $\Delta \tilde{p}$  of the reference solution, respectively defined as

$$\Delta p := p - p_\infty, \quad \Delta \bar{p} := \frac{1}{|\bar{t}|} \int_{\bar{t}} \Delta p dt, \quad \Delta \tilde{p} := \Delta p - \Delta \bar{p},$$

are shown for different angles  $\varphi$  over the polar coordinate  $r$ . These reference results closely match the simulation results of a Direct Numerical Solution (DNS) presented in [39, Figure 8].

To properly quantify the amount of pressure disturbances in the domain, the scaled root-mean-square values of the fluctuating pressure

$$\Delta \tilde{p}_{\text{rms}} = \frac{1}{p_\infty} \sqrt{\frac{1}{\bar{t}} \int_{\bar{t}} \Delta \tilde{p}^2 dt},$$

is computed and compared against the reference solution. In Figure 18 we show a polar plot of the scaled root-mean-square of the fluctuating pressure  $\Delta \tilde{p}_{\text{rms}}$  at two specific shifted radii

$$r_0 = 4.0(1 + \text{Ma}_\infty \cos(\varphi)), \quad r_1 = 7.5(1 + \text{Ma}_\infty \cos(\varphi)),$$

respectively, where the scaling  $(1 + \text{Ma}_\infty \cos(\varphi))$  is known as the Doppler factor [39]. In Figure 19, the contour plot of the scaled root-mean-square of the fluctuating pressure  $\Delta \tilde{p}_{\text{rms}}$  is shown in logarithmic scale.

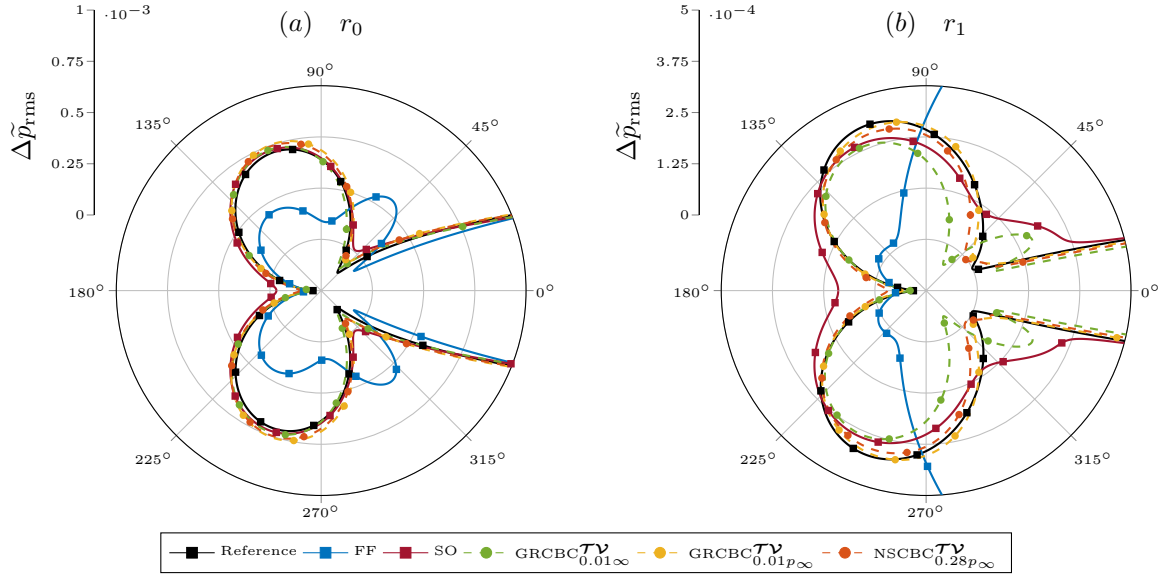


FIGURE 18. Laminar flow around a cylinder: polar plot of the scaled root-mean-square pressure fluctuation  $\Delta\tilde{p}_{\text{rms}}$  for the shifted radii (a)  $r_0$  and (b)  $r_1$ .

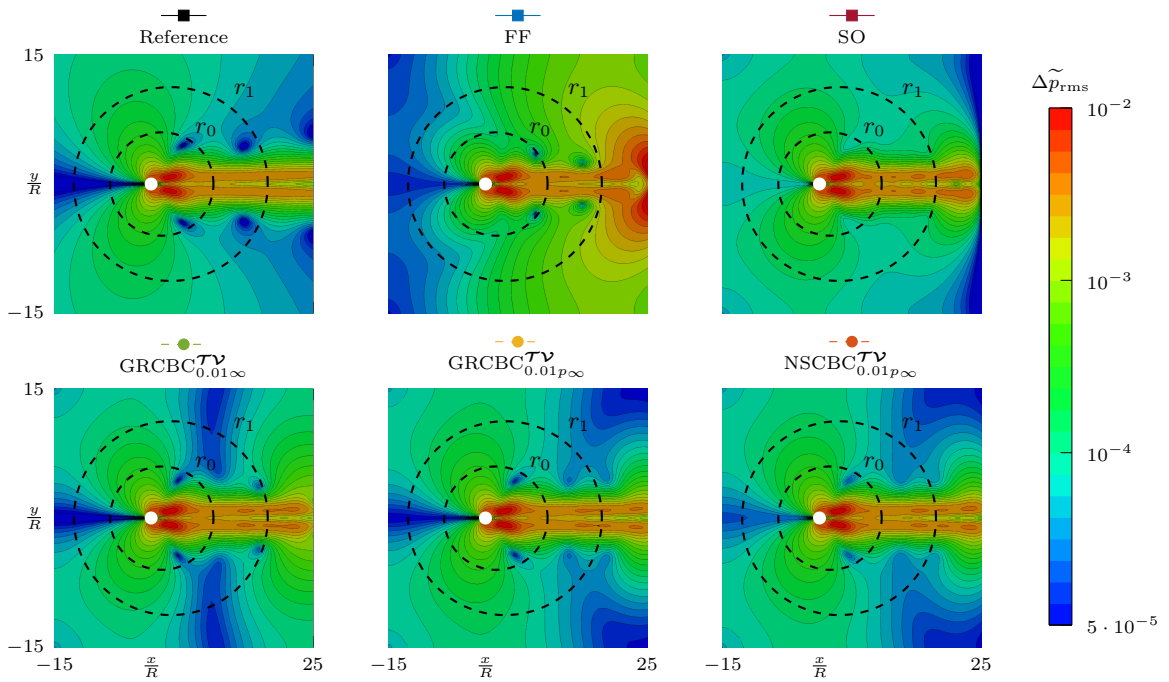


FIGURE 19. Laminar flow around a cylinder: contour plot of the scaled root-mean-square of the fluctuating pressure  $\Delta\tilde{p}_{\text{rms}}$  in logarithmic scale and plot of the shifted circles with radii  $r_0$  and  $r_1$ .

The far-field boundary condition ( $\blacksquare$  FF) shows a vast amount of disturbances propagating upstream, due to vortices crossing the outflow boundary. Similar to the Zero-Circulation Vortex benchmark, the generalized characteristic boundary condition ( $\bullet$  GRCBC $_{0.01\infty}^{\mathcal{T}\nu}$ ) demonstrates a significant improvement compared to ( $\blacksquare$  FF), although, in agreement with the results of [12], performing a relaxation towards the far-field target state  $\mathbf{U}_{\infty}$  at the outflow boundary remains inappropriate. The subsonic outflow boundary condition ( $\blacksquare$  SO) shows a minor deviation from the reference solution upstream of the cylinder ( $\varphi = 180^\circ$ ). This deviation is due to the complete reflection at the subsonic outflow, a phenomenon absent in settings

(-●- GRCBC $_{0.01p_\infty}^{\mathcal{T}\mathcal{V}}$ ) and (-●- NSCBC $_{0.28p_\infty}^{\mathcal{T}\mathcal{V}}$ ). Specifically as the distance from the cylinder increases towards the boundary, we observe a significant deviation from the reference solution for boundary conditions (-■- FF), (-■- SO), and (-●- GRCBC $_{0.01\infty}^{\mathcal{T}\mathcal{V}}$ ). In contrast, the boundary conditions (-●- GRCBC $_{0.01p_\infty}^{\mathcal{T}\mathcal{V}}$ ) and (-●- NSCBC $_{0.28p_\infty}^{\mathcal{T}\mathcal{V}}$ ) demonstrate better agreement due to the inclusion of the transverse  $\mathcal{T}$  and viscous  $\mathcal{V}$  terms, particularly at the shifted radius  $r_1$ .

Lastly, we aim to compute aerodynamic coefficients per unit span, such as the drag coefficient  $c_d$  and lift coefficient  $c_l$ , given their relevance and importance in aerodynamic applications. These quantities are computed via the following expressions

$$\mathbf{F}_{cyl} := \int_{\Gamma_{cyl}} (\boldsymbol{\tau} - p\mathbf{I}) \mathbf{n} ds, \quad c_d := \frac{1}{\frac{1}{2}\rho_\infty u_\infty^2 D} \mathbf{F}_{cyl} \cdot \begin{pmatrix} 1 \\ 0 \end{pmatrix}, \quad c_l := \frac{1}{\frac{1}{2}\rho_\infty u_\infty^2 D} \mathbf{F}_{cyl} \cdot \begin{pmatrix} 0 \\ 1 \end{pmatrix}.$$

Specifically, we are interested in their time-averaged values  $\bar{c}_d, \bar{c}_l$  and first harmonic amplitudes  $\tilde{c}_d, \tilde{c}_l$ , denoted by

$$\bar{c}_d := \frac{1}{\bar{t}} \int_0^{\bar{t}} c_d dt, \quad \bar{c}_l := \frac{1}{\bar{t}} \int_0^{\bar{t}} c_l dt, \quad \tilde{c}_d := \max(c_d - \bar{c}_d), \quad \tilde{c}_l := \max(c_l - \bar{c}_l),$$

respectively. In Table 3, we show the time-averaged drag coefficient  $\bar{c}_d$ , the first harmonic amplitude of the drag coefficient  $\tilde{c}_d$  and lift coefficient  $\tilde{c}_l$ , along with the determined Strouhal number  $St$  for different applied outflow boundary conditions. We omit the time-averaged lift coefficient  $\bar{c}_l$ , as it is zero. Compared to the (-■- Reference) solution every simulation clearly

	$\bar{c}_d$	$\tilde{c}_d$	$\tilde{c}_l$	$St$
-■- Reference	1.333	0.02562	0.5177	0.1822
-■- FF	1.404	0.02688	0.5403	0.1883
-■- SO	1.380	0.02847	0.5106	0.1855
-●- GRCBC $_{0.01\infty}^{\mathcal{T}\mathcal{V}}$	1.402	0.02706	0.5461	0.1883
-●- GRCBC $_{0.01p_\infty}^{\mathcal{T}\mathcal{V}}$	1.392	0.02898	0.5446	0.1872
-●- NSCBC $_{0.28p_\infty}^{\mathcal{T}\mathcal{V}}$	1.388	0.02754	0.5265	0.1864

TABLE 3. Laminar flow around a cylinder: aerodynamic coefficients.

overestimates the drag coefficients  $\bar{c}_d, \tilde{c}_d$ , which can be attributed to the insufficient downstream placement of the outflow boundary relative to the cylinder. For the lift coefficient  $\tilde{c}_l$  and the Strouhal number  $St$ , simulations (-■- SO), (-●- GRCBC $_{0.01p_\infty}^{\mathcal{T}\mathcal{V}}$ ) and (-●- NSCBC $_{0.28p_\infty}^{\mathcal{T}\mathcal{V}}$ ) with the subsonic outflow target state  $\mathbf{U}_{p_\infty}$  show slightly better results than the far-field target state  $\mathbf{U}_\infty$  in simulations (-■- FF) and (-●- GRCBC $_{0.01\infty}^{\mathcal{T}\mathcal{V}}$ ).

We conclude that the newly implemented CBCs significantly reduce pressure disturbances across the domain compared to the commonly used subsonic outflow (-■- SO) and far-field (-■- FF) boundary conditions, while maintaining comparable accuracy of the computed aerodynamic coefficients.

## 6. CONCLUSION

We incorporated the concept of characteristic boundary conditions (CBCs) into the Hybridizable Discontinuous Galerkin (HDG) framework and proposed a new approach to generalized characteristic relaxation boundary conditions (GRCBCs).

The latter include commonly used boundary conditions, such as the subsonic outflow (52) and the far-field (54) boundary condition as special cases, and gives the user the flexibility to tune the relaxation factors to the specific problem under analysis. Most importantly, one can further include tangential and viscous contributions, which show to have a significant impact on the computations in the presented numerical experiments.

The implementation of the CBCs integrates seamlessly into the numerical scheme without the need of additional mirror elements or nodal shape functions as in previous publications in the Discontinuous Galerkin (DG) framework [23, 24, 25].

Through a series of numerical experiments in a weakly compressible setting, we made the following observations:

- For a purely one-dimensional acoustic perturbation (see Subsection 5.1), the far-field target state  $\mathbf{U}_\infty$  acts entirely non-reflecting, regardless of the level of relaxation in the CBCs, making it the most effective target state in this setting. Conversely, fully reflecting target states, such as  $\mathbf{U}_{p_\infty}$ ,  $\mathbf{U}_{\rho u_\infty}$ ,  $\mathbf{U}_{\theta_\infty}$ , can be tuned from partial to zero reflectivity by appropriately adjusting the relaxation parameters.
- For a two-dimensional non-linear pressure pulse injected in a fluid at rest (see Subsection 5.2), the best result was obtained by combining the NSCBC with the subsonic outflow target state  $\mathbf{U}_{p_\infty}$  and the optimal determined [11] relaxation parameter  $\sigma = 0.28$ . However, while the CBCs using the far-field target state  $\mathbf{U}_\infty$  tend to slightly overdamp the perturbation, likely due to the absence of transverse terms, the outcome is comparable to the NSCBC one. Moreover, they are less sensitive to both the relaxation parameter and the alternating inflow and outflow caused by the pulse crossing the boundary.
- For a common scenario in aeroacoustic applications, where vortices cross an artificial outflow boundary (see Subsection 5.3 and Subsection 5.4), the relaxation towards the far-field target state  $\mathbf{U}_\infty$  is inappropriate, in good agreement with [12]. Instead, the CBCs, combined with the subsonic outflow target state  $\mathbf{U}_{p_\infty}$  and the inclusion of transverse terms  $\mathcal{T}$  and viscous terms  $\mathcal{V}$ , show superior performance compared to conventional boundary conditions, both in inviscid and viscous flow scenarios for weakly compressible flow, by minimizing the reflection of vortices at artificial boundaries.

In summary, while the implemented CBCs are not a universal solution and may need to be complemented by other techniques, such as sponge layers or perfectly matched layers, in cases where reflectivity poses a challenge, we conclude that they serve as an effective tool for minimizing reflectivity at artificial boundaries in weakly compressible flow simulations. Particularly, at artificial subsonic outflow boundaries in aeroacoustic simulations, the novel GRCBCs show improved performance compared to common HDG boundary conditions in reducing the reflection of acoustic waves and vortices. As such, they should be preferred over the latter in such scenarios.

## 7. ACKNOWLEDGMENTS

We would like to thank the Austrian Science Fund (FWF) and the Vienna Scientific Cluster (VSC) for their support. This research was funded in whole or in part by the Austrian Science Fund (FWF) [10.55776/P35931]. Calculations were performed using supercomputer resources provided by the Vienna Scientific Cluster (VSC). M.G. and A.H. acknowledge the Spanish Ministry of Science, Innovation and Universities and the Spanish State Research Agency MICIU/AEI/10.13039/501100011033 (Grant agreement No. PID2023-149979OB-I00) and the Generalitat de Catalunya (Grant agreement No. 2021-SGR-01049). M.G. is Fellow of the Serra Hünter Programme of the Generalitat de Catalunya.

## REFERENCES

- [1] Tim Colonius and Sanjiva K. Lele. Computational aeroacoustics: Progress on nonlinear problems of sound generation. *Progress in Aerospace Sciences*, 40(6):345–416, August 2004. ISSN 03760421. doi: 10.1016/j.paerosci.2004.09.001.
- [2] Tim Colonius. Modeling Artificial Boundary Conditions for Compressible Flow. *Annual Review of Fluid Mechanics*, 36(1):315–345, January 2004. ISSN 0066-4189, 1545-4479. doi: 10.1146/annurev.fluid.36.050802.121930.
- [3] Tim Colonius. Boundary conditions for turbulence simulation. In *Numerical Methods in Turbulence Simulation*, pages 319–357. Elsevier, 2023. ISBN 978-0-323-91144-3. doi: 10.1016/B978-0-32-391144-3.00014-0.
- [4] Daniel J. Bodony. Analysis of sponge zones for computational fluid mechanics. *Journal of Computational Physics*, 212(2):681–702, March 2006. ISSN 00219991. doi: 10.1016/j.jcp.2005.07.014.

- [5] Ali Mani. Analysis and optimization of numerical sponge layers as a nonreflective boundary treatment. *Journal of Computational Physics*, 231(2):704–716, January 2012. ISSN 0021-9991. doi: 10.1016/j.jcp.2011.10.017.
- [6] Fang Q. Hu, X.D. Li, and D.K. Lin. Absorbing boundary conditions for nonlinear Euler and Navier–Stokes equations based on the perfectly matched layer technique. *Journal of Computational Physics*, 227(9):4398–4424, April 2008. ISSN 00219991. doi: 10.1016/j.jcp.2008.01.010.
- [7] Fang Q. Hu. Development of PML absorbing boundary conditions for computational aeroacoustics: A progress review. *Computers & Fluids*, 37(4):336–348, May 2008. ISSN 00457930. doi: 10.1016/j.compfluid.2007.02.012.
- [8] G.W Hedstrom. Nonreflecting boundary conditions for nonlinear hyperbolic systems. *Journal of Computational Physics*, 30(2):222–237, February 1979. ISSN 00219991. doi: 10.1016/0021-9991(79)90100-1.
- [9] Kevin W Thompson. Time dependent boundary conditions for hyperbolic systems. *Journal of Computational Physics*, 68(1):1–24, January 1987. ISSN 00219991. doi: 10.1016/0021-9991(87)90041-6.
- [10] Kevin W Thompson. Time-dependent boundary conditions for hyperbolic systems, II. *Journal of Computational Physics*, 89(2):439–461, August 1990. ISSN 00219991. doi: 10.1016/0021-9991(90)90152-Q.
- [11] David H. Rudy and John C. Strikwerda. A nonreflecting outflow boundary condition for subsonic navier-stokes calculations. *Journal of Computational Physics*, 36(1):55–70, June 1980. ISSN 00219991. doi: 10.1016/0021-9991(80)90174-6.
- [12] Sergio Pirozzoli and Tim Colonius. Generalized characteristic relaxation boundary conditions for unsteady compressible flow simulations. *Journal of Computational Physics*, 248: 109–126, September 2013. ISSN 00219991. doi: 10.1016/j.jcp.2013.04.021.
- [13] T.J Poinso and S.K Lelef. Boundary conditions for direct simulations of compressible viscous flows. *Journal of Computational Physics*, 101(1):104–129, 1992. ISSN 0021-9991. doi: 10.1016/0021-9991(92)90046-2.
- [14] C. S. Yoo, Y. Wang, A. Trouvé, and H. G. Im. Characteristic boundary conditions for direct simulations of turbulent counterflow flames. *Combustion Theory and Modelling*, 9 (4):617–646, November 2005. ISSN 1364-7830, 1741-3559. doi: 10.1080/13647830500307378.
- [15] Guido Lodato. *Conditions Aux Limites Tridimensionnelles Pour La Simulation Directe et Aux Grandes Échelles Des Écoulements Turbulents. Modélisation de Sous-Maille Pour La Turbulence En Région de Proche Paroi*. PhD thesis, December 2008.
- [16] Guido Lodato, Pascale Domingo, and Luc Vervisch. Three-dimensional boundary conditions for direct and large-eddy simulation of compressible viscous flows. *Journal of Computational Physics*, 227(10):5105–5143, May 2008. ISSN 00219991. doi: 10.1016/j.jcp.2008.01.038.
- [17] Qianlong Liu and Oleg V. Vasilyev. Nonreflecting boundary conditions based on nonlinear multidimensional characteristics. *International Journal for Numerical Methods in Fluids*, 62(1):24–55, January 2010. ISSN 02712091, 10970363. doi: 10.1002/fld.2011.
- [18] Nicolas Odier, Marlène Sanjosé, Laurent Gicquel, Thierry Poinso, Stéphane Moreau, and Florent Duchaine. A characteristic inlet boundary condition for compressible, turbulent, multispecies turbomachinery flows. *Computers & Fluids*, 178:41–55, January 2019. ISSN 0045-7930. doi: 10.1016/j.compfluid.2018.09.014.
- [19] Guido Lodato, Frank Ham, and Heinz Pitsch. Optimal Inclusion of Transverse Effects in the NonReflecting Outflow Boundary Condition. *AIAA Journal*, August 2012. doi: 10.2514/1.J051318.
- [20] Bernardo Cockburn. Discontinuous Galerkin Methods for Computational Fluid Dynamics. In *Encyclopedia of Computational Mechanics Second Edition*, pages 1–63. John Wiley & Sons, Ltd, 2017. ISBN 978-1-119-17681-7. doi: 10.1002/9781119176817.ecm2053.
- [21] Chi-Wang Shu. Discontinuous Galerkin Method for Time-Dependent Problems: Survey and Recent Developments. In Xiaobing Feng, Ohannes Karakashian, and Yulong Xing, editors, *Recent Developments in Discontinuous Galerkin Finite Element Methods for Partial Differential Equations*, volume 157, pages 25–62. Springer International Publishing, Cham,

2014. ISBN 978-3-319-01817-1 978-3-319-01818-8. doi: 10.1007/978-3-319-01818-8\_2.
- [22] Daniele Antonio Di Pietro and Alexandre Ern. *Mathematical Aspects of Discontinuous Galerkin Methods*, volume 69 of *Mathématiques et Applications*. Springer Berlin Heidelberg, Berlin, Heidelberg, 2012. ISBN 978-3-642-22979-4 978-3-642-22980-0. doi: 10.1007/978-3-642-22980-0.
- [23] Ioannis Touloupoulos and John A. Ekaterinaris. Artificial boundary conditions for the numerical solution of the Euler equations by the discontinuous galerkin method. *Journal of Computational Physics*, 230(15):5974–5995, July 2011. ISSN 00219991. doi: 10.1016/j.jcp.2011.04.008.
- [24] Edmond K. Shehadi and Edwin T.A. Van Der Weide. A polynomial-correction Navier-Stokes characteristic boundary condition. *Computer Physics Communications*, 303:109194, October 2024. ISSN 00104655. doi: 10.1016/j.cpc.2024.109194.
- [25] Edmond Shehadi. *Non-Reflecting Boundary Conditions in the Context of the Discontinuous Galerkin Finite Element Method*. PhD thesis, University of Twente, Enschede, The Netherlands, May 2024.
- [26] Jaime Peraire, Ngoc Nguyen, and Bernardo Cockburn. A Hybridizable Discontinuous Galerkin Method for the Compressible Euler and Navier-Stokes Equations. In *48th AIAA Aerospace Sciences Meeting Including the New Horizons Forum and Aerospace Exposition*, Orlando, Florida, January 2010. American Institute of Aeronautics and Astronautics. ISBN 978-1-60086-959-4. doi: 10.2514/6.2010-363.
- [27] N.C. Nguyen and J. Peraire. Hybridizable discontinuous Galerkin methods for partial differential equations in continuum mechanics. *Journal of Computational Physics*, 231(18): 5955–5988, July 2012. ISSN 00219991. doi: 10.1016/j.jcp.2012.02.033.
- [28] B. Cockburn, N.C. Nguyen, and J. Peraire. HDG Methods for Hyperbolic Problems. In *Handbook of Numerical Analysis*, volume 17, pages 173–197. Elsevier, 2016. ISBN 978-0-444-63789-5. doi: 10.1016/bs.hna.2016.07.001.
- [29] Bernardo Cockburn. Static Condensation, Hybridization, and the Devising of the HDG Methods. In Gabriel R. Barrenechea, Franco Brezzi, Andrea Cangiani, and Emmanuil H. Georgoulis, editors, *Building Bridges: Connections and Challenges in Modern Approaches to Numerical Partial Differential Equations*, volume 114, pages 129–177. Springer International Publishing, Cham, 2016. ISBN 978-3-319-41638-0 978-3-319-41640-3. doi: 10.1007/978-3-319-41640-3\_5.
- [30] Charles Hirsch. *Numerical Computation of Internal and External Flows. 2: Computational Methods for Inviscid and Viscous Flows*. A Wiley Interscience Publication. Wiley, Chichester, repr edition, 2002. ISBN 978-0-471-92452-4 978-0-471-92351-0.
- [31] Axel Rohde. Eigenvalues and eigenvectors of the Euler equations in general geometries. In *15th AIAA Computational Fluid Dynamics Conference*, Anaheim, CA, U.S.A., June 2001. American Institute of Aeronautics and Astronautics. doi: 10.2514/6.2001-2609.
- [32] Culbert B. Laney. *Computational Gasdynamics*. Cambridge University Press, 1 edition, June 1998. ISBN 978-0-521-57069-5 978-0-521-62558-6 978-0-511-60560-4. doi: 10.1017/CBO9780511605604.
- [33] C. S. Yoo and H. G. Im. Characteristic boundary conditions for simulations of compressible reacting flows with multi-dimensional, viscous and reaction effects. *Combustion Theory and Modelling*, 11(2):259–286, April 2007. ISSN 1364-7830. doi: 10.1080/13647830600898995.
- [34] Jordi Vila-Pérez, Matteo Giacomini, Ruben Sevilla, and Antonio Huerta. Hybridizable discontinuous Galerkin formulation of compressible flows. *Archives of Computational Methods in Engineering*, 28(2):753–784, March 2021. ISSN 1134-3060, 1886-1784. doi: 10.1007/s11831-020-09508-z.
- [35] Jaime Peraire, Cuong Nguyen, and Bernardo Cockburn. An Embedded Discontinuous Galerkin Method for the Compressible Euler and Navier-Stokes Equations. In *20th AIAA Computational Fluid Dynamics Conference*, Honolulu, Hawaii, June 2011. American Institute of Aeronautics and Astronautics. ISBN 978-1-62410-148-9. doi: 10.2514/6.2011-3228.
- [36] Matteo Giacomini, Ruben Sevilla, and Antonio Huerta. Tutorial on Hybridizable Discontinuous Galerkin (HDG) formulation for incompressible flow problems. In L. De Lorenzis

- and A. Düster, editors, *Modeling in Engineering Using Innovative Numerical Methods for Solids and Fluids*, volume 599 of *CISM International Centre for Mechanical Sciences*, pages 163–201. Springer International Publishing, 2020. doi: 10.1007/978-3-030-37518-8\_5.
- [37] Joachim Schoberl. C++11 Implementation of Finite Elements in NGSolve. Research Report ASC Report 30/2014, Institute of Analysis and Scientific Computing, TU Wien, Wien, 2014.
- [38] Jan Ellmenreich, Matteo Giacomini, Antonio Huerta, and Philip L. Lederer. Simulation data for the paper ”Characteristic boundary conditions for Hybridizable Discontinuous Galerkin methods”, March 2025.
- [39] Osamu Inoue and Nozomu Hatakeyama. Sound generation by a two-dimensional circular cylinder in a uniform flow. *Journal of Fluid Mechanics*, 471:285–314, November 2002. ISSN 0022-1120, 1469-7645. doi: 10.1017/S0022112002002124.

INSTITUTE OF ANALYSIS AND SCIENTIFIC COMPUTING, TU WIEN, WIEDNER HAUPTSTRASSE 8-10, 1040 WIEN  
*Email address:* `jan.ellmenreich@tuwien.ac.at`

FACHBEREICH MATHEMATIK, UNIVERSITÄT HAMBURG, BUNDESSTRASSE 55, 20146 HAMBURG, GERMANY  
*Email address:* `philip.lederer@uni-hamburg.de`

(UPC) LABORATORI DE CÀLCUL NUMÈRIC (LACÀN), ETS DE INGENIERÍA DE CAMINOS, CANALES Y PUERTOS, UNIVERSITAT POLITÈCNICA DE CATALUNYA, BARCELONA, SPAIN.

(CIMNE) CENTRE INTERNACIONAL DE MÈTODES NUMÈRICS EN ENGINYERIA (CIMNE), BARCELONA, SPAIN.  
*Email address:* `matteo.giacomini@upc.edu`

(UPC) LABORATORI DE CÀLCUL NUMÈRIC (LACÀN), ETS DE INGENIERÍA DE CAMINOS, CANALES Y PUERTOS, UNIVERSITAT POLITÈCNICA DE CATALUNYA, BARCELONA, SPAIN.

(CIMNE) CENTRE INTERNACIONAL DE MÈTODES NUMÈRICS EN ENGINYERIA (CIMNE), BARCELONA, SPAIN.  
*Email address:* `antonio.huerta@upc.edu`